AD-A174 235 ACOUSTIC SCATTERING KERNELS FROM ARCTIC SEA ICE(U) 1/1
SCIENCE APPLICATIONS INTERNATIONAL CORP MCLEAN VA
D RUBENSTEIN OCT 86 SAIC-86/1077 N00014-84-C-0180
UNCLASSIFIED F/G 20/1 NL

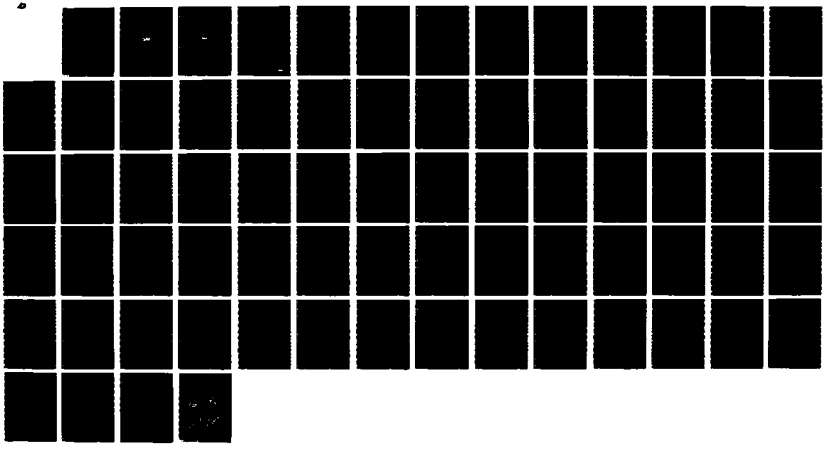

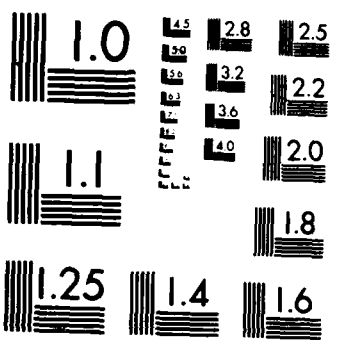

ACOUSTIC SCATTERING KERNELS FROM ARCTIC SEA ICE

SAIC-86/1077

ACOUSTIC SCATTERING KERNELS FROM ARCTIC SEA ICE

SAIC-86/1077

SAIC™
Science Applications International Corporation

Post Office Box 1303, 1710 Goodridge Drive, McLean, Virginia 22102, (703) 821-4300

ACOUSTIC SCATTERING KERNELS FROM ARCTIC SEA ICE

SAIC-86/1077

October 1986

Prepared by:

David Rubenstein

Prepared for:

Mr. E.D. Chaika
Mr. B.N. Wheatley
AEAS Program
ONR Detachment, Code 132

Contract No. N00014-84-C-0180

SCIENCE APPLICATIONS INTERNATIONAL CORPORATION

1710 Goodridge Drive
P.O. Box 1303
McLean, Virginia 22102
(703) 821-4300

UNCLASSIFIED

SECURITY CLASSIFICATION OF THIS PAGE (When Data Entered)

REPORT DOCUMENTATION PAGE	READ INSTRUCTIONS BEFORE COMPLETING FORM
1. REPORT NUMBER: SAIC-86/1077	2. GOVT ACCESSION NO.: AD-A174235
3. RECIPIENT'S CATALOG NUMBER:	
4. TITLE (and Subtitle): Acoustic Scattering Kernels from Arctic Sea Ice	5. TYPE OF REPORT & PERIOD COVERED: Technical Report
	6. PERFORMING ORG. REPORT NUMBER: SAIC-86/1077
7. AUTHOR(s): David Rubenstein	8. CONTRACT OR GRANT NUMBER(s): N00014-84-C-0180
9. PERFORMING ORGANIZATION NAME AND ADDRESS: Science Applications International Corp. 1710 Goodridge Dr., P.O. Box 1303 McLean, VA 22102	10. PROGRAM ELEMENT, PROJECT, TASK AREA & WORK UNIT NUMBERS: Task 27.2
11. CONTROLLING OFFICE NAME AND ADDRESS: AEAS Program, ONR Detachment, Code 132 NSTL, MS 39529	12. REPORT DATE: October 1986
	13. NUMBER OF PAGES:
14. MONITORING AGENCY NAME & ADDRESS(if different from Controlling Office):	15. SECURITY CLASS. (of this report): Unclassified
	15a. DECLASSIFICATION/DOWNGRADING SCHEDULE:

16. DISTRIBUTION STATEMENT (of this Report)

Unlimited

17. DISTRIBUTION STATEMENT (of the abstract entered in Block 20, if different from Report)

18. SUPPLEMENTARY NOTES

19. KEY WORDS (Continue on reverse side if necessary and identify by block number)

Arctic, Scatter, Acoustic, Ice, Keel, Ridge

20. ABSTRACT (Continue on reverse side if necessary and identify by block number)

A new algorithm for computing scattering kernels from Arctic ice keels is described. The basic equations are adapted from Burke and Twersky (1966) but the algorithm does not involve approximations in the limits of low or high frequencies, and is therefore more accurate. Calculations over a range of frequencies and grazing angles are presented. An important result is obtained. At high frequencies (greater than 200 Hz) a significant component of the incoherent scattered energy is directed into shallow propagation angles (less

DD FORM 1 JAN 73 1473 EDITION OF 1 NOV 55 IS OBSOLETE

UNCLASSIFIED

SECURITY CLASSIFICATION OF THIS PAGE (When Data Entered)

20. Abstract (Continued)

than 15 degrees). This component must be accounted for in estimates of scattering loss.

TABLE OF CONTENTS

LIST OF FIGURES

LIST OF FIGURES (Continued)

Section 1
INTRODUCTION

The Arctic ice-covered environment presents a sort of surface scattering that is quite different from that in the open ocean. Under-ice acoustic propagation undergoes incoherent scattering in the presence of ice keels. Greene and Bowen (1983) reviewed the special environmental conditions that differentiate acoustic propagation in the Arctic from open ocean regions. The under-ice roughness associated with ice keels has a very important effect on sound propagation. Greene (1984) developed a statistical model of under-ice roughness, based on a distribution of randomly oriented cylindrical keels. Using this model, Greene developed an interim scattering model (SISM/ICE), which is a hybrid of theories based on continuous and discrete roughness models. This type of characterization of scattering is important for the Navy's propagation models. Rubenstein et al. (1986) described an implementation of SISM/ICE for the ASTRAL and PE models. The concepts are also relevant to other models, including FACT, FFP, MPP, and RAYMODE.

The SISM/ICE model is probably adequate for low frequencies, below about 200 Hz. However, at higher frequencies, SISM/ICE ignores the scattered, incoherent component of energy that is directed within the sound channel (Greene and Rubenstein, 1986). Therefore, a more realistic scattering kernel is needed for higher frequency applications. In this report, an algorithm is described for computing realistic scattering kernels for a field of ice keels.

The under-ice surface is considered to be flat, with cylindrical bosses of elliptical cross section. The basic assumptions are that the ice keels

(1) have a constant size, and a half-width-to-depth ratio of 1.6, as suggested by Diachok (1976),

(2) have random orientation,

(3) have random spacing with uniform distribution along a track, and that

(4) pressure release boundary conditions are appropriate.

Section 2 of this report describes the model equations in some detail. The basic equations are from Burke and Twersky (1966). A new method of calculation is described in Section 3. The method involves a direct calculation of power series of Mathieu functions, and is more accurate than the approximate methods of Burke and Twersky. Section 4 presents results of applying the model to determine reflection coefficients, scattering cross sections, and scattering losses for particular fields of ice keels.

Section 2
MODEL EQUATIONS

2.1 MATHIEU'S EQUATIONS AND MATHIEU FUNCTIONS

The elliptic coordinate system is a natural one to use for the problem of scattering off an elliptical cylinder. Following the notation from Morse and Feshbach (1953), the coordinates μ and θ are related to Cartesian coordinates by

$$x = 1/2\ a \cosh \mu \cos\theta,$$
$$y = 1/2\ a \sinh \mu \sin\theta, \tag{2.1}$$

where a curve μ = constant is an ellipse and a curve θ = constant is a hyperbola, each with foci at $x = \pm 1/2$ a. See Figure 2.1 for a schematic drawing. For reference, the elliptic coordinates are related to polar coordinates by

$$r = 1/2\ a \left[\cosh^2 \mu - \sin^2\theta\right]^{1/2},$$
$$\phi = \tan^{-1} \left[\tanh \mu \tan\theta\right]. \tag{2.2}$$

In Cartesian coordinates, the Helmholtz wave equation is written

$$\left(\frac{\partial^2}{\partial x^2} + \frac{\partial^2}{\partial y^2} + k^2\right) \psi = 0, \tag{2.3}$$

and transforming to elliptic coordinates, the equation becomes

$$\frac{\partial^2 \psi}{\partial \mu^2} + \frac{\partial^2 \psi}{\partial \theta^2} + h^2 (\cosh^2 \mu - \cos^2\theta)\psi = 0, \tag{2.4}$$

where

$$h = \frac{1}{2} ak, \tag{2.5}$$

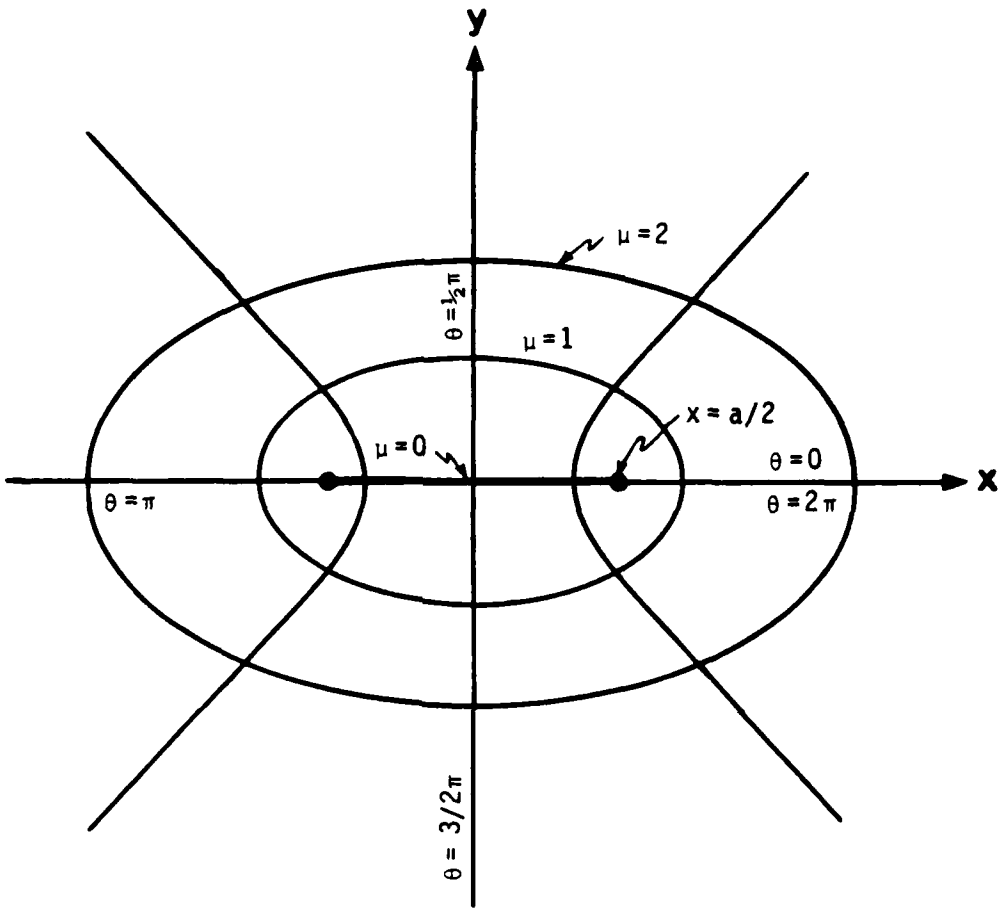

Figure 2.1. Elliptic Coordinate System, μ and θ.

$k = 2\pi/\lambda$ is the wavenumber, and λ is wavelength. Eq. (2.4) separates into two ordinary differential equations

$$\frac{d^2H}{d\theta^2} + (b - h^2\cos^2\theta)H = 0 \ , \tag{2.6}$$

$$-\frac{d^2M}{d\mu^2} + (b - h^2\cosh^2\mu)M = 0, \tag{2.7}$$

with

$$\psi = H(\theta)\ M(\mu) \ . \tag{2.8}$$

Eq. (2.6) is Mathieu's equation, and (2.7) is known as Mathieu's modified equation.

The solutions to (2.6) are periodic in θ. The solutions

$$Se_m\ (h,\theta) = \sum_{n=0}^{\infty} A_n\ (h,m)\ \cos\ (n\theta) \ ,$$

$$So_m\ (h,\theta) = \sum_{n=1}^{\infty} B_n\ (h,m)\ \sin\ (n\theta) \ , \tag{2.9}$$

are even and odd functions, respectively, about $\theta=0$. Those functions with even order m have period π, and those with odd order m have period 2π. Also, the even order functions are even about $\theta = \pi/2$ and $3\pi/2$, and the odd order functions are odd there.

The Fourier coefficients in (2.9) are normalized as

$$\sum_{n=0}^{\infty} A_n = 1 \ ,$$

$$\sum_{n=1}^{\infty} n\ B_n = 1 \ . \tag{2.10}$$

In addition, normalization constants are defined by

$$Me_m(h) = \int_0^{2\pi} Se_m(h,\theta)^2 \, d\theta$$

$$= 2\pi \sum_{n=0}^{\infty} \frac{1}{\epsilon_n} A_n(h,m)^2 ,$$

$$Mo_m(h) = \int_0^{2\pi} So_m(h,\theta)^2 \, d\theta$$

$$= \pi \sum_{n=1}^{\infty} B_n(h,m)^2 , \qquad (2.11)$$

where $\epsilon_n = 1$ for $n = 0$, and $\epsilon_n = 2$ for $n > 0$.

Solutions to the modified equation (2.7) may be written

$$Je_{2m}(h,\mu) = \sqrt{\frac{\pi}{2}} \sum_{n=0}^{\infty} (-1)^{n-m} A_{2n} J_{2n}(h \cosh\mu) ,$$

$$Je_{2m+1}(h,\mu) = \sqrt{\frac{\pi}{2}} \sum_{n=0}^{\infty} (-1)^{n-m} A_{2n+1} J_{2n+1}(h \cosh\mu) ,$$

$$Jo_{2m}(h,\mu) = \sqrt{\frac{\pi}{2}} \tanh\mu \sum_{n=1}^{\infty} (-1)^{n-m} 2nB_{2n} J_{2n}(h \cosh\mu) ,$$

$$Jo_{2m+1}(h,\mu) = \sqrt{\frac{\pi}{2}} \tanh\mu \sum_{n=0}^{\infty} (-1)^{n-m}(2n+1)B_{2n+1}J_{2n+1}(h \cosh\mu), \qquad (2.12)$$

where J_n are Bessel functions, and Je and Jo are radial Mathieu functions of the first kind. Radial functions of the second kind Ne and No can be obtained by replacing the J_n in (2.12) with Neumann functions N_n, and by changing the lower summation limit for No from 1 to 0. Radial functions of the third kind He and Ho are analogous to Hankel functions,

$$He_n = Je_n + i\, Ne_n,$$

$$Ho_n = Jo_n + i\, No_n. \tag{2.13}$$

2.2 SCATTERING SOLUTION

We develop the solution for plane waves scattered by a semi-elliptical cylinder. In terms of Mathieu functions, a plane wave is expressed by

$$\psi_i = e^{ikr\cos(u-\phi)} = e^{ik\,(x\cos u + y\sin u)}$$

$$= \sqrt{8\pi} \sum_{n=0}^{\infty} \sum_{j=e,o} i^n \frac{Sj_n(h,u)Sj_n(h,\theta)}{Mj_n(h)} Jj_n(h,\mu), \tag{2.14}$$

where the summation variable j indicates a summation over even and odd Mathieu functions, and the subscript i denotes a wave that is incident on a cylindrical surface.*

The scattered wave ψ_s (see Figure 2.2) is represented in terms of outgoing radial Mathieu functions,

$$\psi_s = \sqrt{8\pi} \sum_{n=0}^{\infty} \sum_{j=e,o} i^n\, Xj_n \frac{Sj_n(h,u)Sj_n(h,\theta)}{Mj_n(h)} Hj_n(h,\mu)\ , \tag{2.15}$$

where the coefficients Xj_n are determined by the boundary conditions. We use a free surface boundary condition,

$$\psi_i + \psi_s = 0\ . \tag{2.16}$$

---

* This expression for ψ_i is the same as that quoted by Morse and Feshbach (1953), but is different from that quoted by Burke and Twersky (1964) by a factor $\sqrt{\pi/2}$. However, a second discrepancy in Burke and Twersky (1964) in their asymptotic expression for radial Mathieu functions He_m and Ho_m compensates exactly, so that the later results fall into agreement.

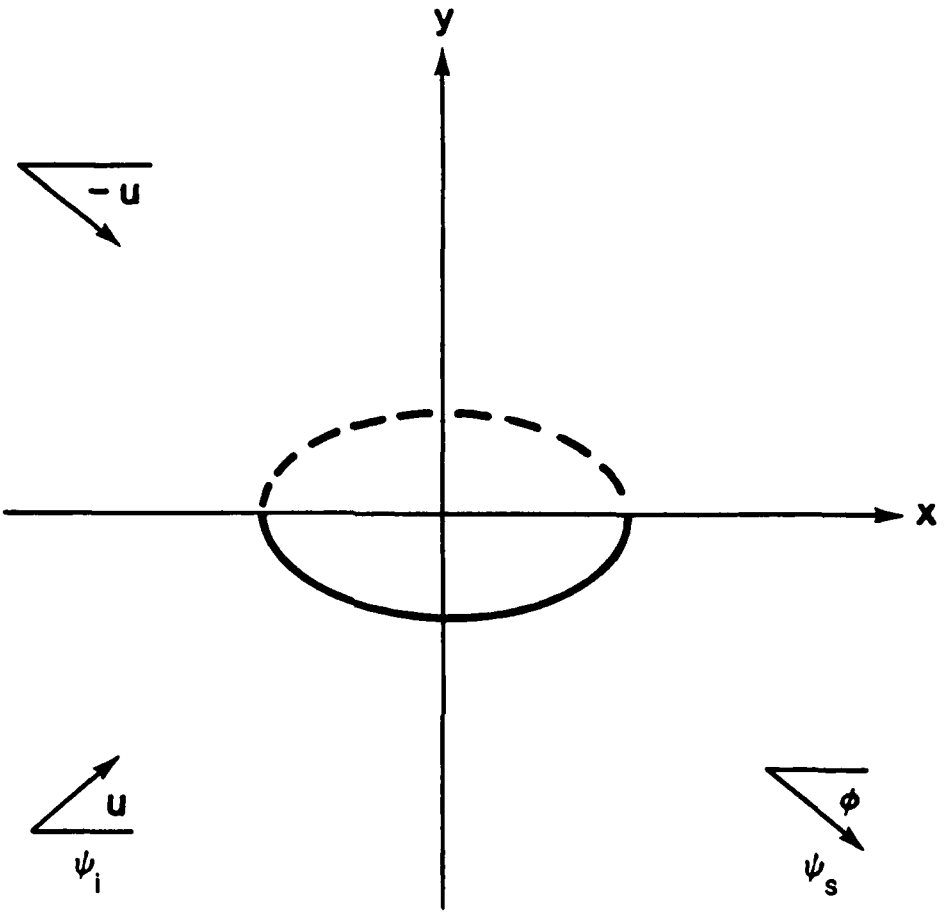

Figure 2.2. Diagram of elliptical cross section of cylinder in the lower half-plane, incoming grazing angle u and outgoing angle ϕ. The angle -u corresponds to virtual image plane wave.

Therefore, the coefficients become

$$Xj_n = -\frac{Jj_n(h,\mu_o)}{Hj_n(h,\mu_o)} , \tag{2.17}$$

where $\mu = \mu_o$ is the surface of the elliptical cylinder.

To obtain the solution for a semi-elliptical cylinder, we use Rayleigh's image technique. We superpose two incident waves from directions u and -u, and compute the total scattered field. Because of the symmetry properties of periodic Mathieu functions,

$$Se_n(u) = Se_n(-u) ,$$

$$So_n(u) = -So_n(-u) , \tag{2.18}$$

the total scattered field becomes

$$\Psi = \psi_s(u) - \psi_s(-u)$$

$$= 2\sqrt{8\pi} \sum_{n=0}^{\infty} i^n Xo_n \frac{So_n(h,u)\, So_n(h,\theta)}{Mo_n(h)} Ho_n(h,\mu) . \tag{2.19}$$

We can derive an approximation to (2.19) which is accurate in the far field. Using the asymptotic formulas

$$So_n(h,\theta) \to So_n(h,\phi) ,$$

$$Ho_n(h,\mu) \to \sqrt{\frac{1}{ikr}}\, e^{ikr}\, i^{-n} , \tag{2.20}$$

we write

$$\Psi \simeq \sqrt{\frac{2}{i\pi kr}}\, e^{ikr}\, f(\phi,u), \tag{2.21}$$

where

$$f(\phi,u) = 4\pi \sum_{n=0}^{\infty} Xo_n \frac{So_n(h,u)\ So_n(h,\phi)}{Mo_n(h)} \quad . \tag{2.22}$$

We have written the function $f(\phi,u)$ in a form comparable to the f_- function used by Burke and Twersky (1964, 1966), with u and ϕ being the incoming and outgoing grazing angles, respectively. The normalization constants $Mo_n(h)$ are defined as in Morse and Feshbach (1953) and Burke and Twersky (1966), but are different from those used by Burke and Twersky (1964) by a factor 2π. We also note that our angles here are grazing angles, whereas in Burke and Twersky (1964, 1966) they are incident.

We call the case treated here oblate, because the ground plane y=0 is aligned parallel to the elliptical cylinder's major axis. Because of the symmetry of this case, the even Mathieu functions have dropped out of (2.19) and (2.22). The prolate case, in which the major axis is aligned perpendicular to the ground plane, is also treated by Burke and Twersky (1964, 1966). Because it is not specifically of interest to the ice keel scattering problem, it is not included here. The expressions analogous to (2.19) and (2.22) for the prolate case involve summations over odd-order even periodic Mathieu functions and even-order odd periodic Mathieu functions.

2.3 GRID OF RANDOMLY DISTRIBUTED SCATTERERS

Here the equations for a grid of randomly distributed ice keels (semi-elliptical cylinders) are summarized, from Burke and Twersky (1966). We define a quantity

$$Z = \frac{n}{k \sin u} f(u,u) \quad , \tag{2.23}$$

where n is the number density of scatterers per unit length. Then the coherent power reflection coefficient is given by

$$R = \left|\frac{1+Z}{1-Z}\right|^2 . \tag{2.24}$$

The incoherent scattering cross section per unit length is written

$$\sigma(\phi,u) = \frac{2n}{\pi k} \left|\frac{f(\phi,u)}{1-Z}\right|^2 . \tag{2.25}$$

Conservation of energy may be expressed by

$$R + \csc(u) \int_0^{\pi} \sigma(\phi,u)\, d\phi = 1 , \tag{2.26}$$

that is, coherent reflected energy, plus the integral of incoherent scattered energy, equals the total incident energy.

Section 3

METHOD OF CALCULATION

Burke and Twersky (1966) used approximate methods for computing the scattering solutions. Their approximations are valid in the limits of low and high frequencies.

Instead of using these approximate methods, we calculated the reflection coefficient R and scattering cross section σ directly, by explicitly evaluating the power series (2.22).

The algorithm developed by Clemm (1969) was used to compute the periodic and radial Mathieu functions. This algorithm uses trigonometric function power series for computing periodic Mathieu functions, and Bessel function power series for computing radial Mathieu functions. In computing these power series, a tolerance level of 10^{-13} is set. The power series is truncated when the magnitudes of two successive terms, relative to the magnitude of the largest term, is less than or equal to the tolerance level. Test cases were run, comparing computed values of Mathieu functions with values tabulated in Abramowitz and Stegun (1964). Agreement was good to seven decimal places. In order to achieve agreement with Morse and Feshbach (1953), it is necessary to choose the Ince normalization option in Clemm's (1969) algorithm for the radial Mathieu functions, and to multiply the computed values by a factor $\sqrt{\pi/2}$.

The power series in (2.22) was explicitly evaluated, up to a truncation order. This truncation order was reached when its addition changed the summation value, in a relative sense, less than a given tolerance level. This tolerance level was 10^{-4}.

As a check on the correctness of the solutions, qualitative comparisons of R and σ results with figures in Burke and Twersky (1966)

were performed. As a quantitative check, the expression (2.26) for energy conservation was evaluated. The integral over outgoing angles was evaluated using a simple trapezoidal numerical integration. The average resolution from 0 to π was about 5°, with 2° resolution in the vicinity of the main scattering lobe. The error was found to be on the order of 1%. Better accuracy might be achieved by improving the angular resolution in the numerical integration, or by decreasing the tolerance level in the summation of (2.22). Of course, both approaches would lead to increased computational expense.

Section 4

RESULTS

This section presents results for calculations of coherent power reflection coefficient R, and scattering cross section σ. For these calculations we make certain assumptions concerning ice keel shapes and distributions. We assume that keels have a half-width-to-depth ratio of 1.6, that they have a random orientation, and that they are spaced randomly along a track. Consider the assumption that keels have random orientation. Even if the ice field contains keels of only a single size, the projected keel width intercepted by any particular track will take on a range of values. The average projected keel width will be equal to the actual keel width times a factor $\pi/2$. If the keels are spaced randomly, then we can attribute an average separation distance to an ice keel field.

Figure 4.1 shows reflection loss as a function of grazing angle, for three frequencies; 50, 100, and 200 Hz. The keel depth is 4.3 m. Therefore the keel width is 13.76 m, and the average projected width is 21.61 m. We assume an average keel separation distance of 92 m. The 200 Hz curve increases most rapidly with grazing angle, because its small wavelength (7.5 m) is best able to resolve the keel shape. The curve reaches a peak at 30°, and then falls as shadowing decreases and more flat surface becomes illuminated. Qualitatively similarly shaped curves were presented by Burke and Twersky (1966).

Figures 4.2 - 4.12 show scattering cross section σ as a function of scattered angle, for different frequencies, ranging from 20 Hz to 3500 Hz. Each figure shows four incoming grazing angles; 5°, 10°, 15°, and 20°, signified by small arrows on the left side of each plot. The reader should note that the radial coordinate axes have different scales on each of the plots.

At 20 Hz and 50 Hz, a single main scattering lobe appears in each plot. Secondary lobes begin to appear at 100 Hz and above. At high frequencies, the secondary lobe structures become quite complicated. The main scattering lobes increase in magnitude with increasing frequency and with increasing grazing angle. They also become more narrow with increasing frequency.

The orientations of the main lobes decrease in angle with increasing frequency. Above about 250 Hz, the orientation angle also increases with incoming grazing angle. At the highest frequencies, the lobes are oriented at angles nearly equal to their respective incoming grazing angles. In other words, at high frequencies, most of the scattered energy is directed into the same angle as that of coherent specular reflection.

We computed the surface scattering loss coefficient SL, given by

$$SL = 1 - R - \csc(u) \int_0^{\phi_L} \sigma(\phi,u)d\phi = \csc(u) \int_{\phi_L}^{\pi} \sigma(\phi,u)d\phi \ . \qquad (4.1)$$

Note the difference between the ranges of integration in (4.1) and (2.26). The range from 0 to ϕ_L is the angular range of propagation in the Arctic Ocean. Energy directed below $\phi_L \approx 15°$, represented by the last term in (4.1), is eventually absorbed by bottom loss. Figures 4.13 and 4.14 show R and 1-SL as a function of frequency, for grazing angles u = 5° and u = 10°, respectively. These figures show that at frequencies below 200 Hz, the coherent power reflection loss is a good estimator of scattering loss. However, above 200 Hz R and 1-SL begin to diverge. The reason is that a significant fraction of the scattered energy is directed within the angular range of propagation, from 0° to 15°. Therefore, it is necessary to evaluate the full expression (4.1) for an accurate estimate of scattering loss at high frequencies.

Figures 4.15 - 4.24 show the scattering cross section σ, in a manner analogous to Figs. 4.2 - 4.12, for a different set of keel parameters. The frequencies range from 20 Hz to 1600 Hz. The parameters for this case are: keel depth = 7.7 m, average projected width = 38.7 m, average separation = 62 m. This case gives results that are qualitatively similar to those of the first case. Quantitatively, the magnitude of σ is greater for this second case, because of the larger size and denser concentration of keel cylinders.

The results may be summarized as follows:

1) At low frequencies, below about 200 Hz, most of the incoherent, scattered energy is directed into large angles with respect to the horizontal, and therefore exits from the sound propagation channel.

2) With increasing frequency, the orientation angle of the main lobe of the scattering cross section asymptotically approaches the incident grazing angle. Above 200 Hz, a significant fraction of the incoherent, scattered energy is directed into shallow propagation angles, less than 15°.

For realistic predictions, acoustic propagation models must incorporate these effects. This was done, for example, in an energy transport model described by Greene and Rubenstein (1986). This transport model, in fact, includes azimuthal as well as vertical angle scattering cross sections. This approach allows a more general three-dimensional prediction of propagation.

(This page is blank)

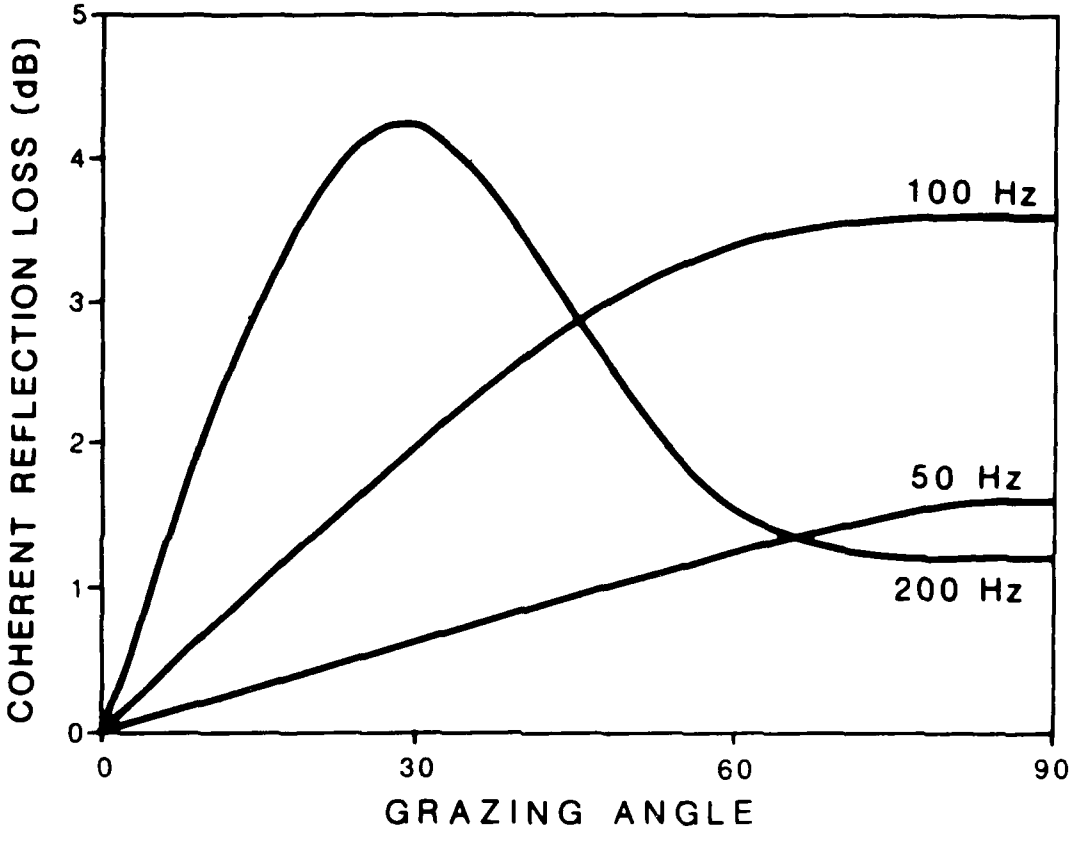

Figure 4.1. Reflection Coefficient R for Frequencies 50, 100, and 200 Hz.

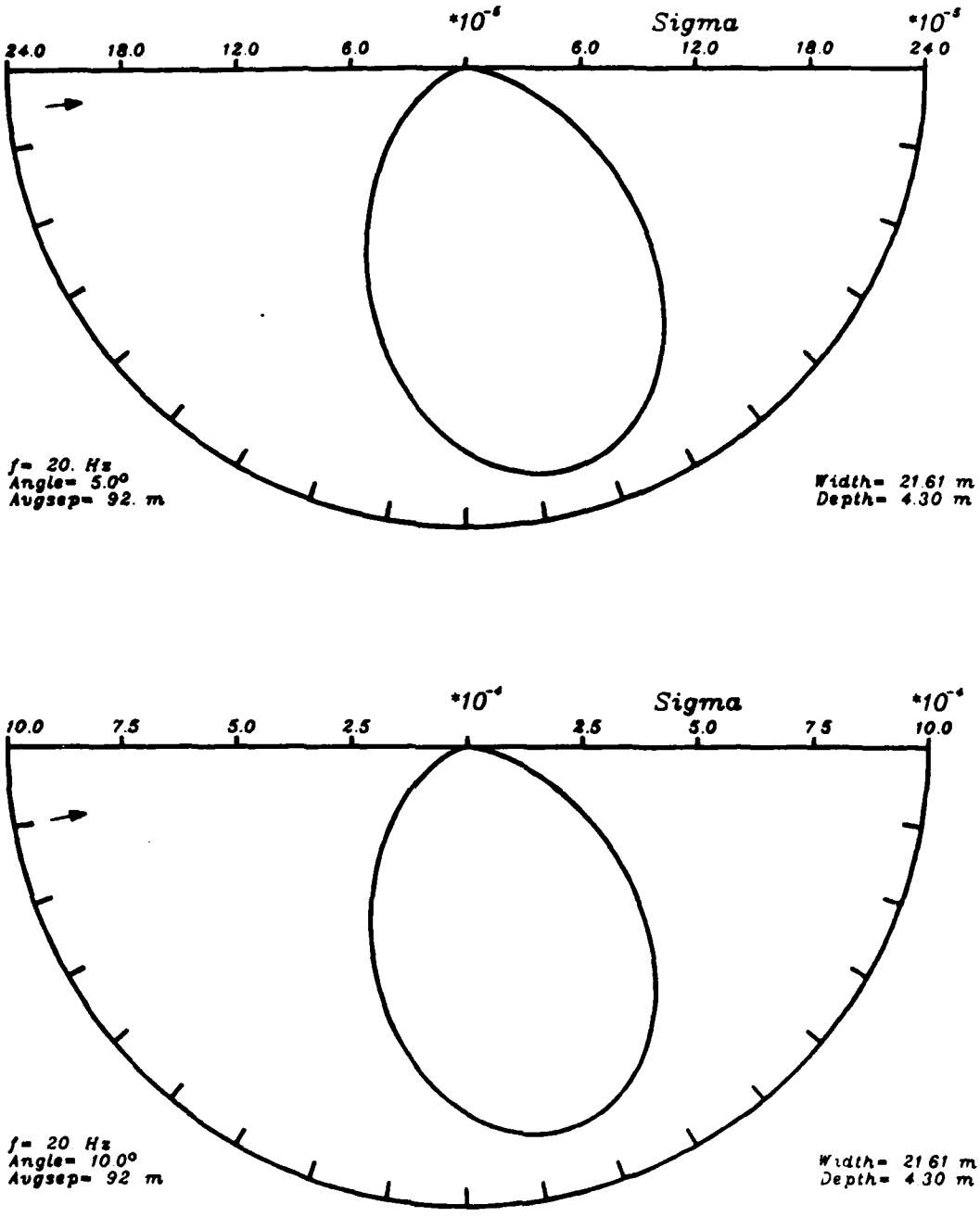

Figure 4.2. Scattering cross sections at 20 Hz. Incoming grazing angles are 5°, 10°, 15°, and 20°. Keel parameters: Width = 21.61 m, Depth = 4.3 m, Average Separation = 92 m.

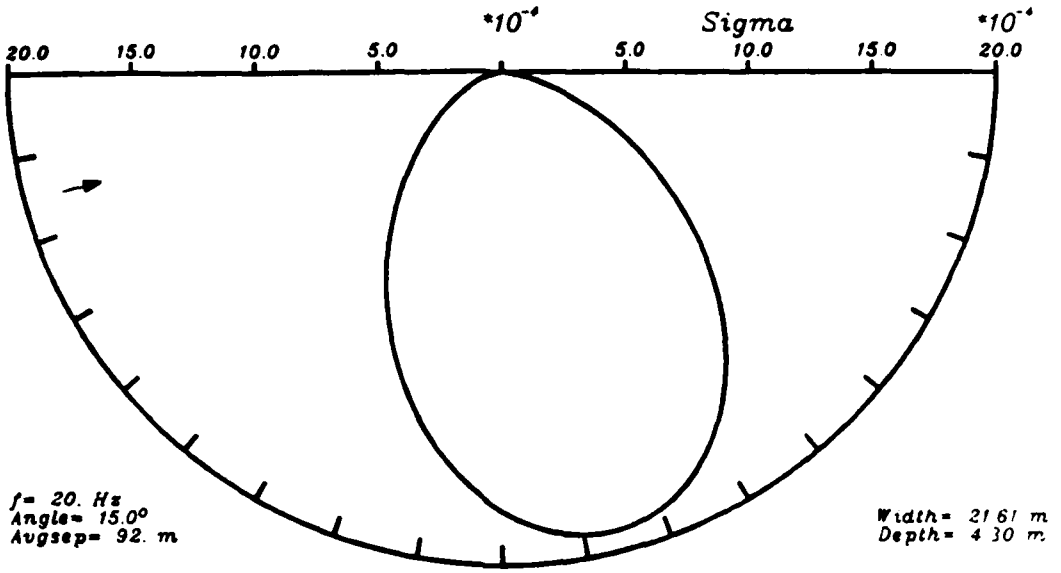

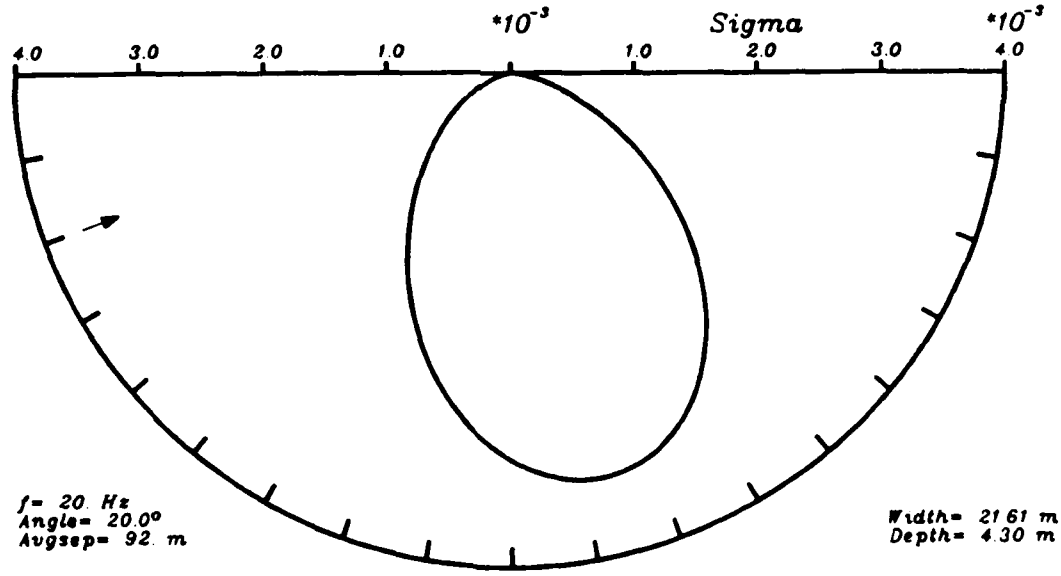

Figure 4.2. (Continued)

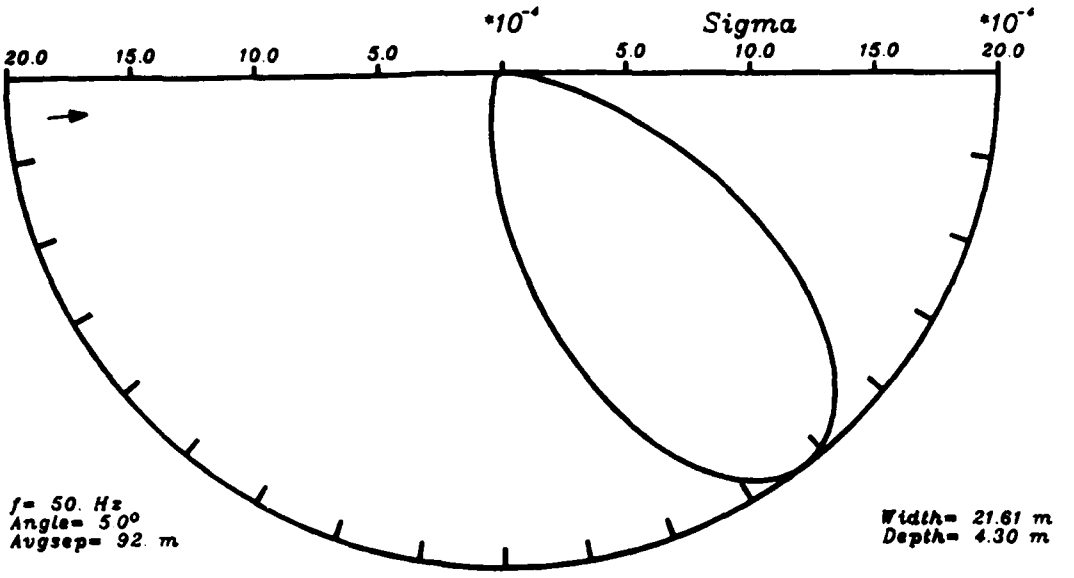

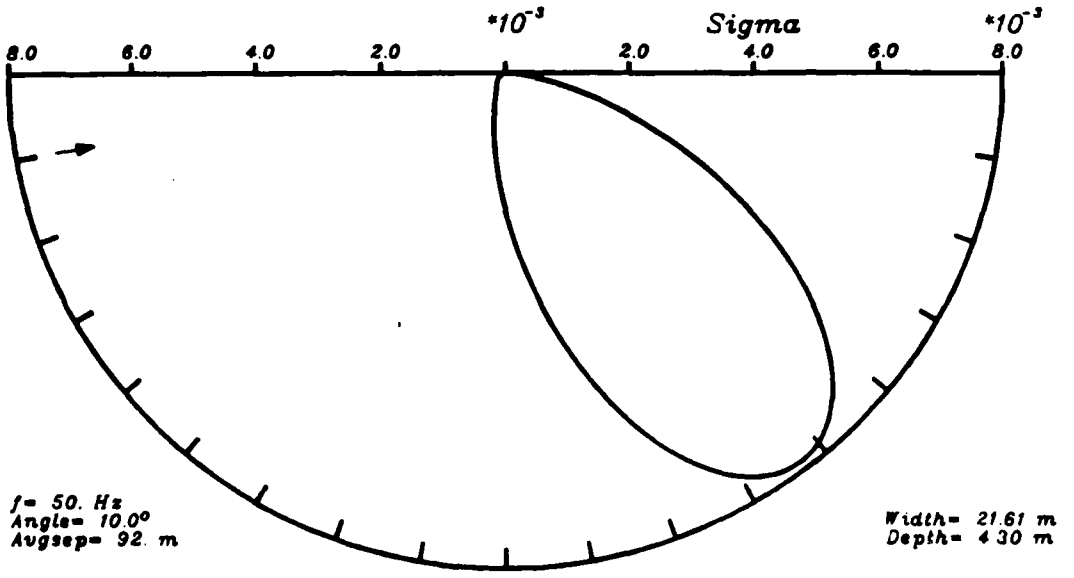

Figure 4.3. As in Figure 4.2, but at 50 Hz.

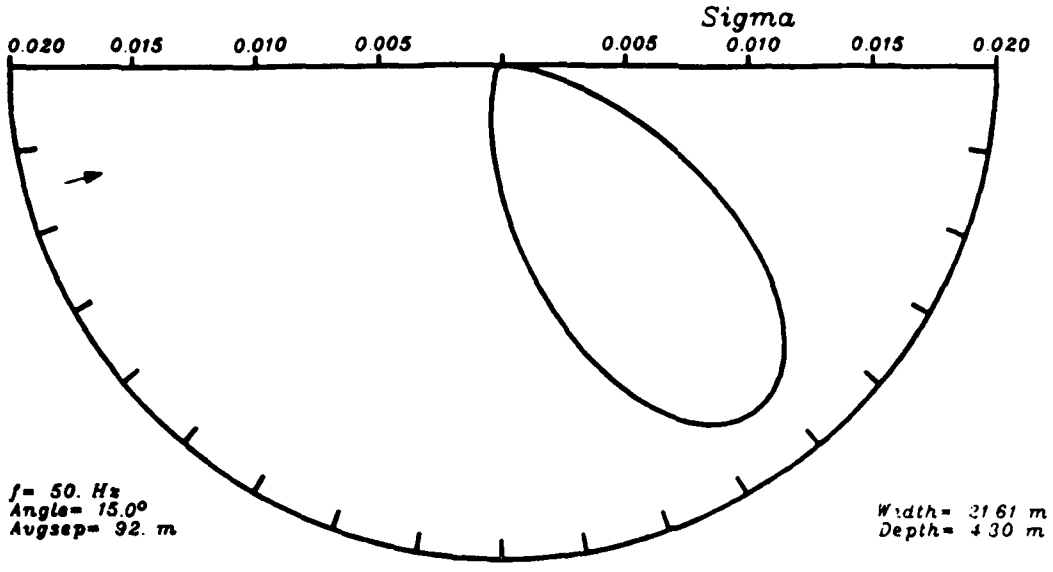

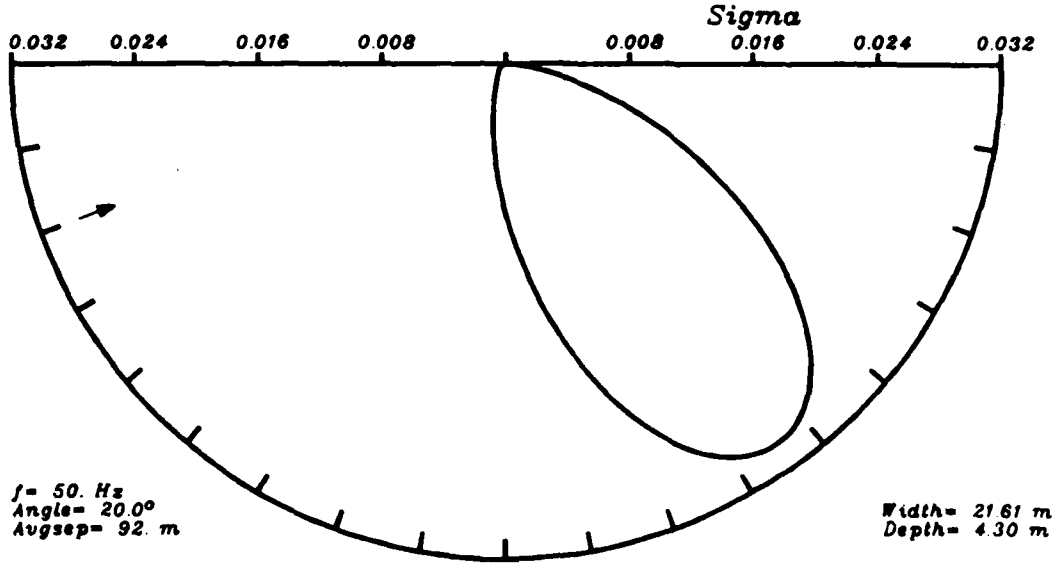

Figure 4.3. (Continued)

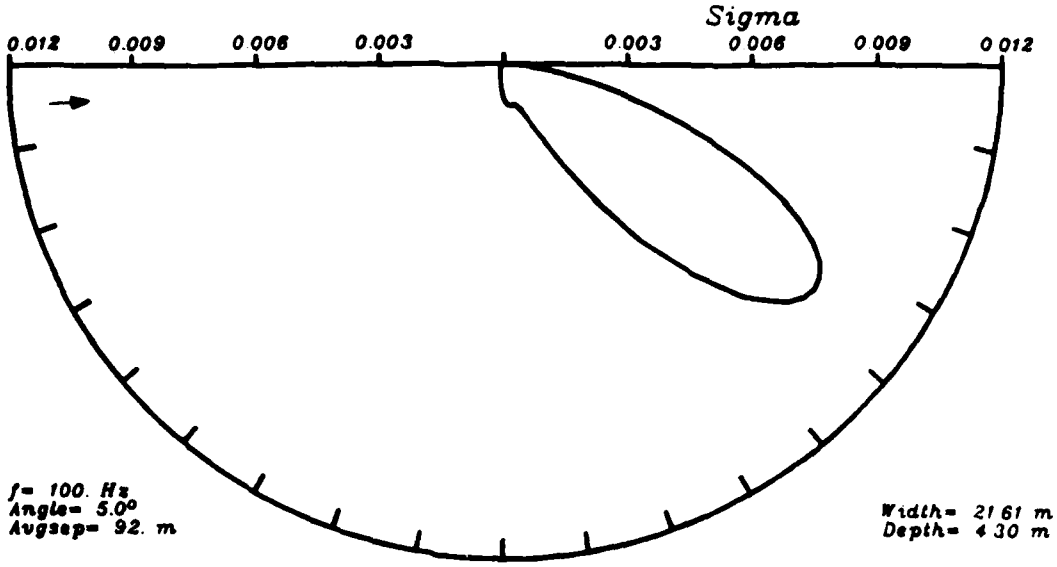

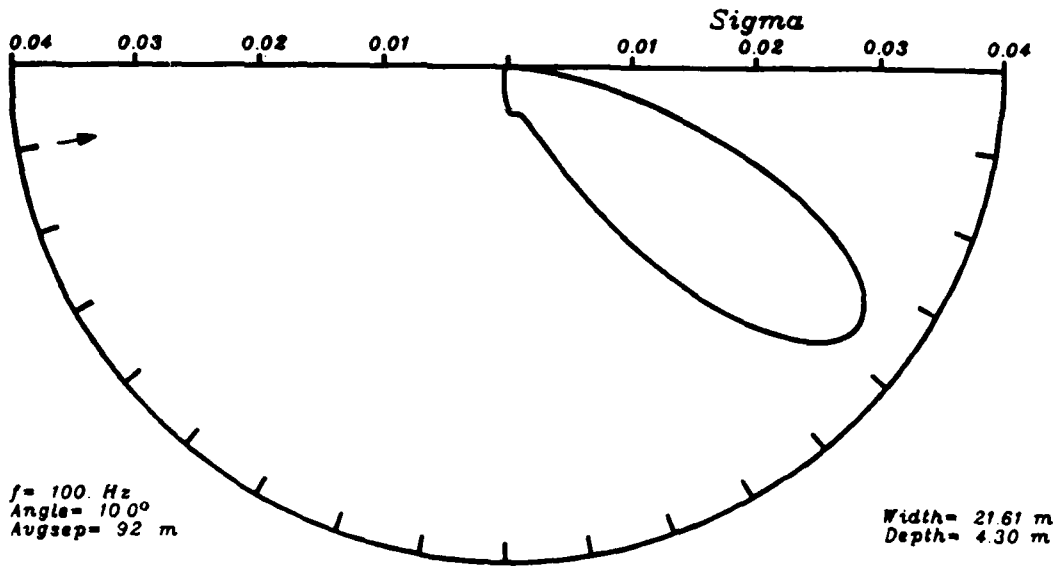

Figure 4.4. As in Figure 4.2, but at 100 Hz.

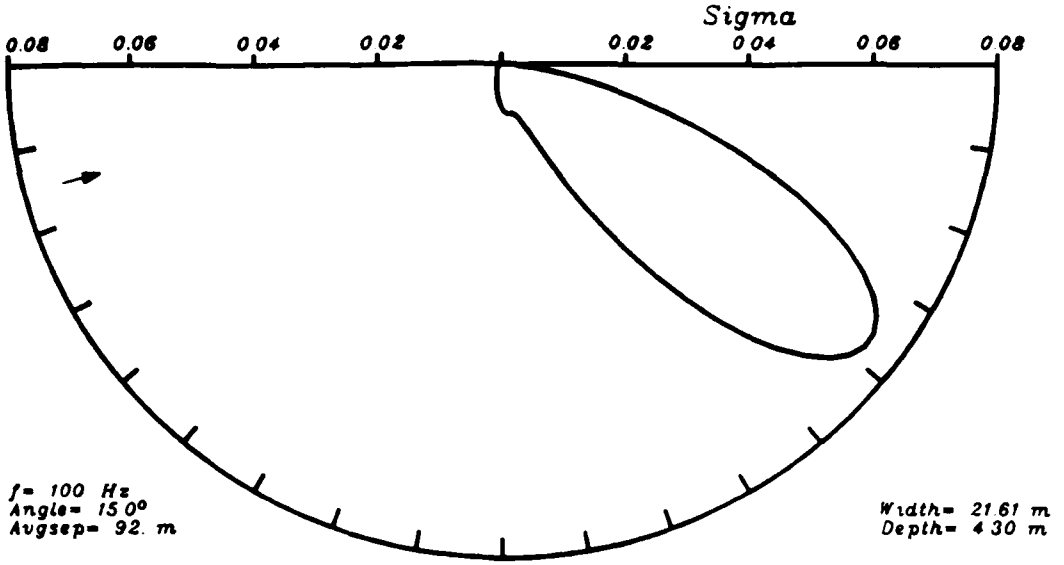

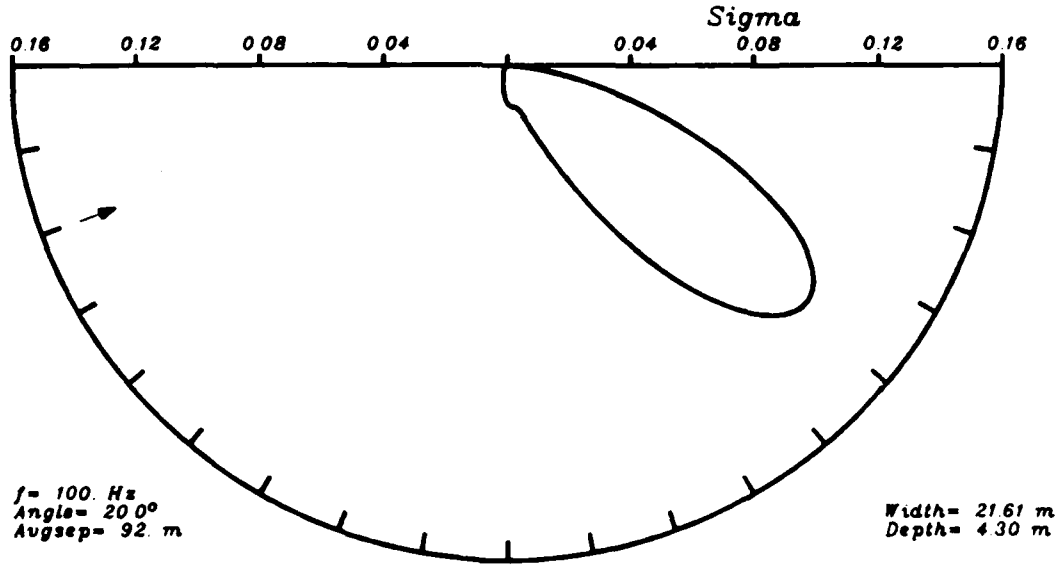

Figure 4.4. (Continued)

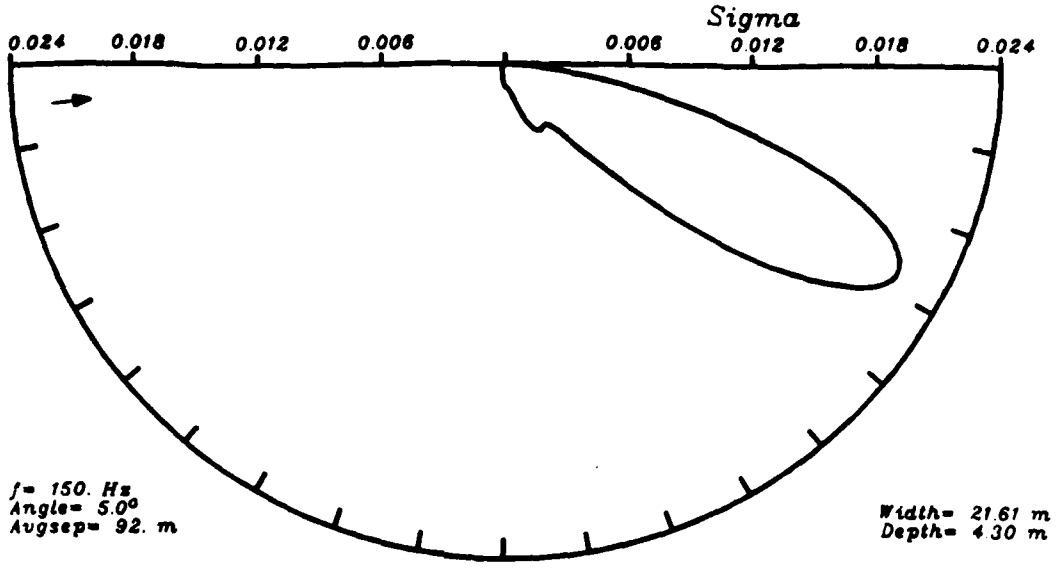

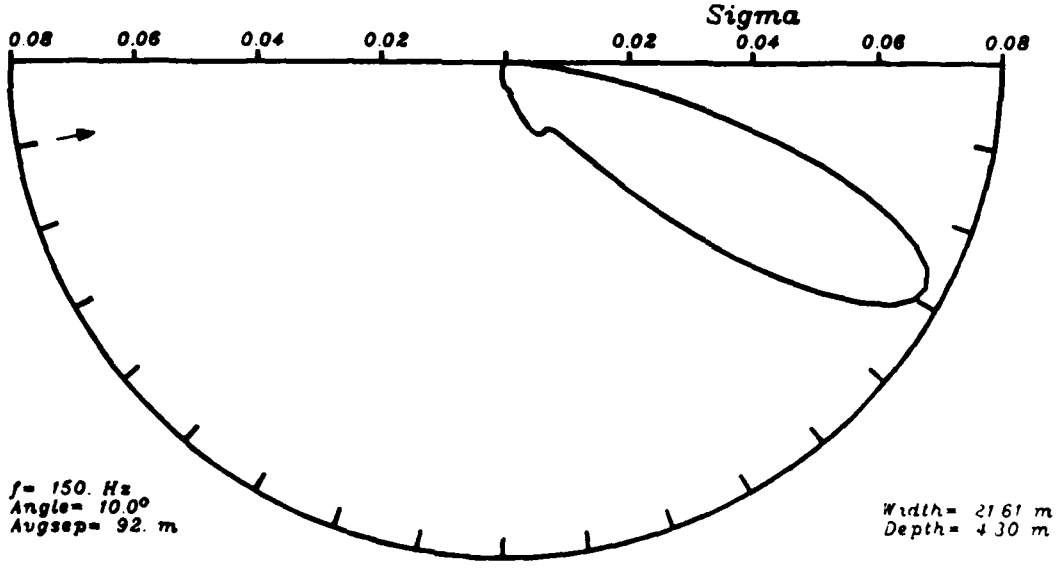

Figure 4.5. As in Figure 4.2, but at 150 Hz.

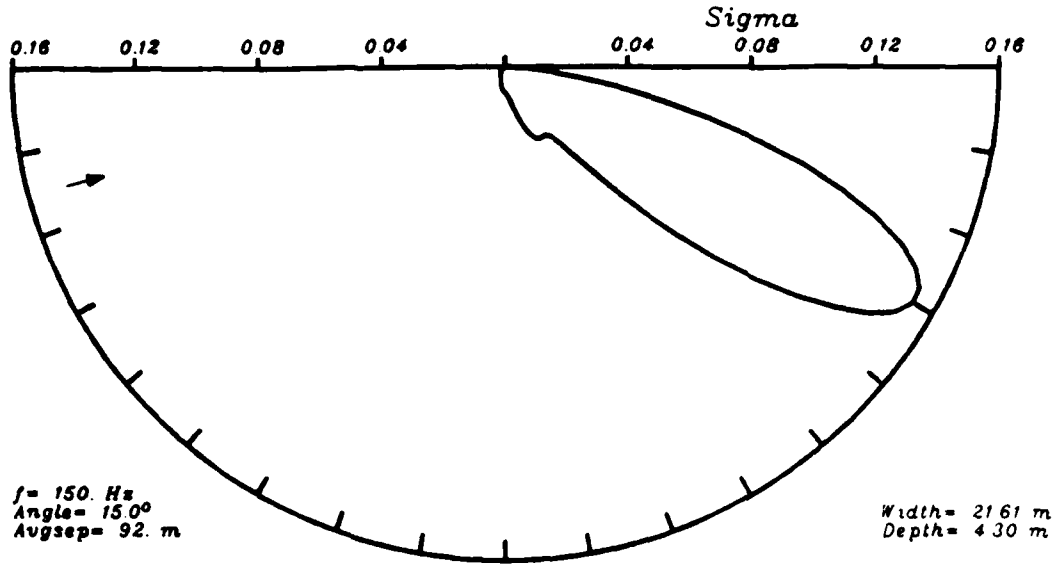

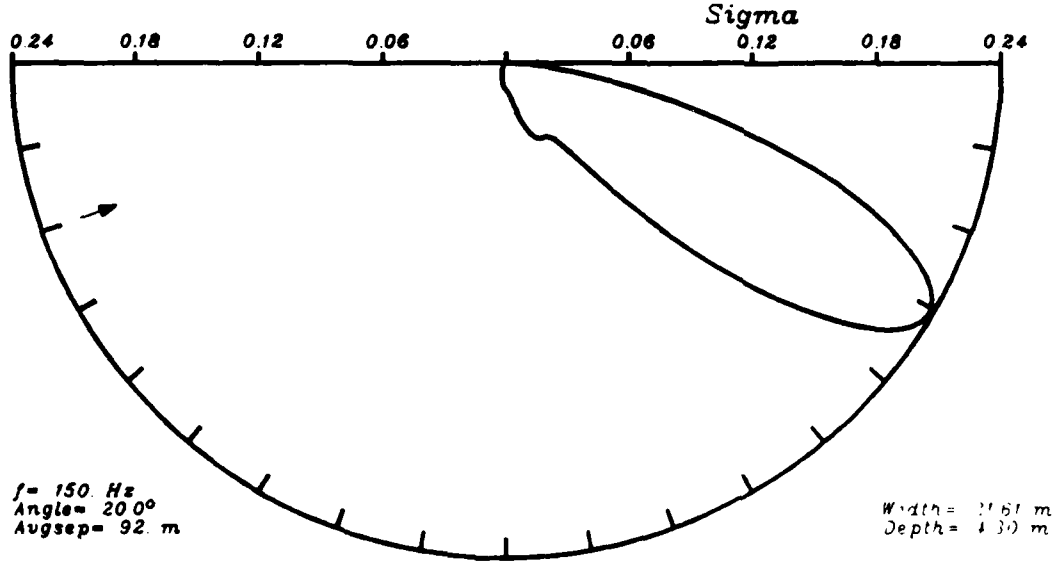

Figure 4.5. (Continued)

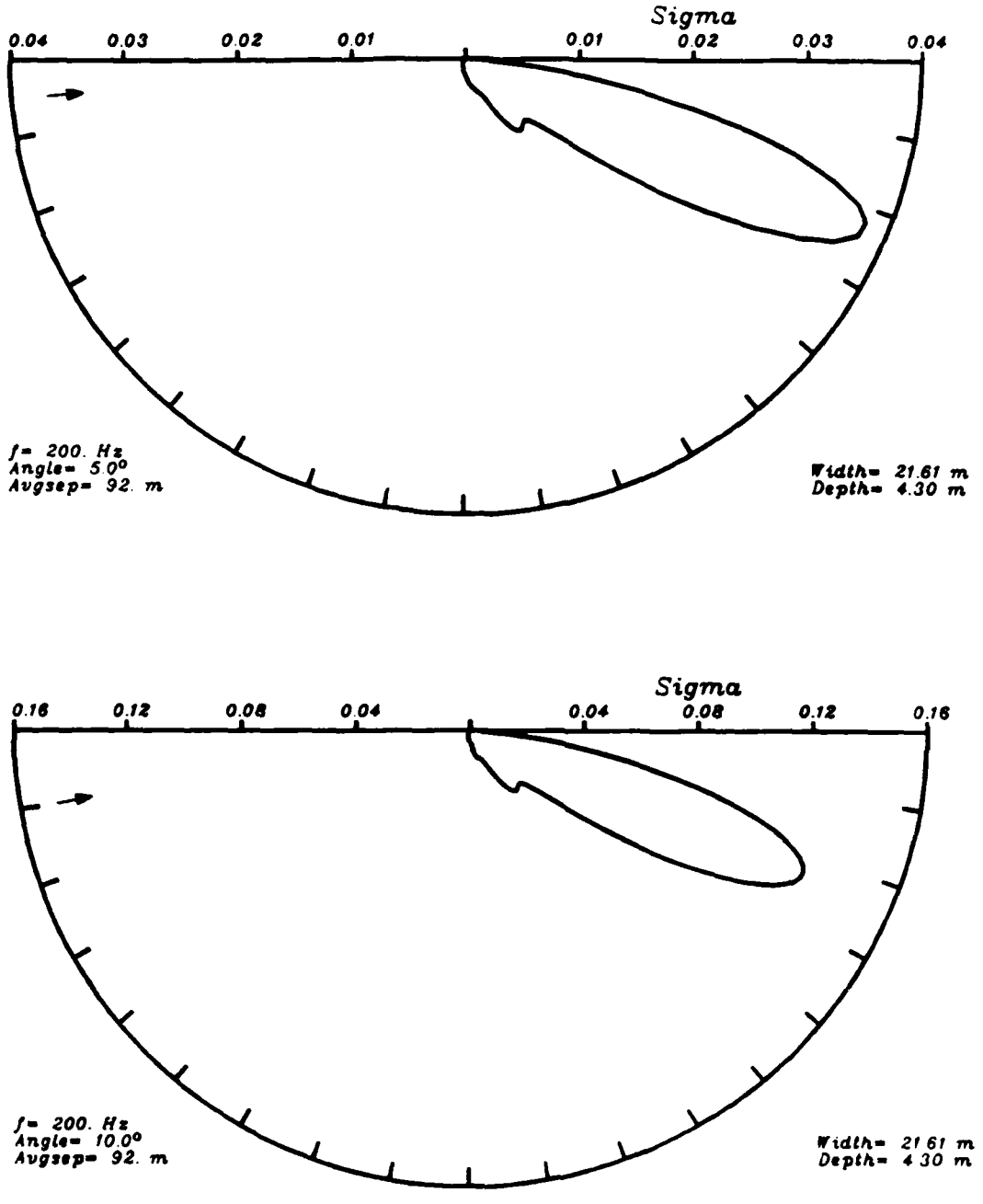

Figure 4.6. As in Figure 4.2, but at 200 Hz.

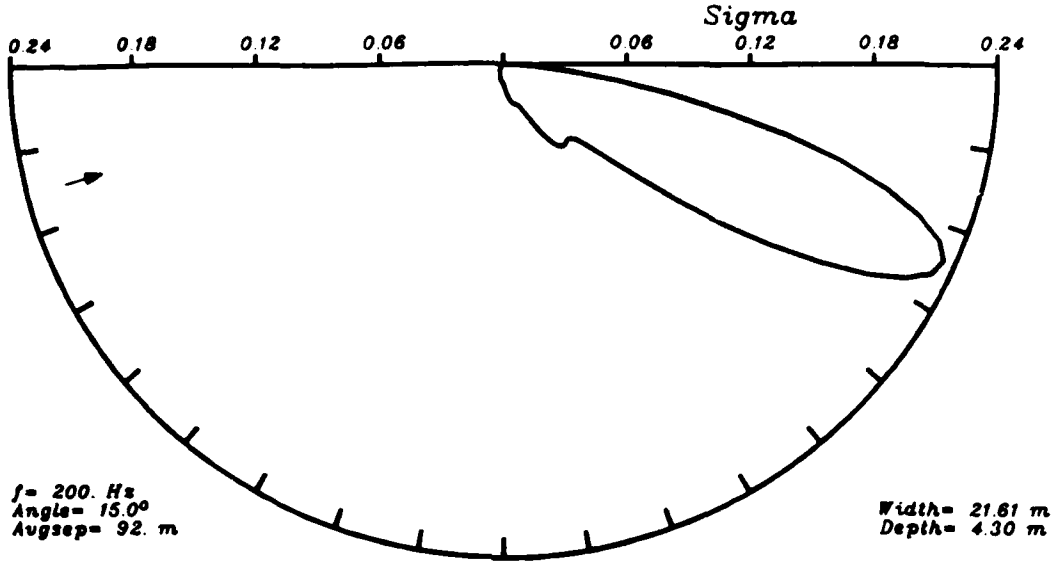

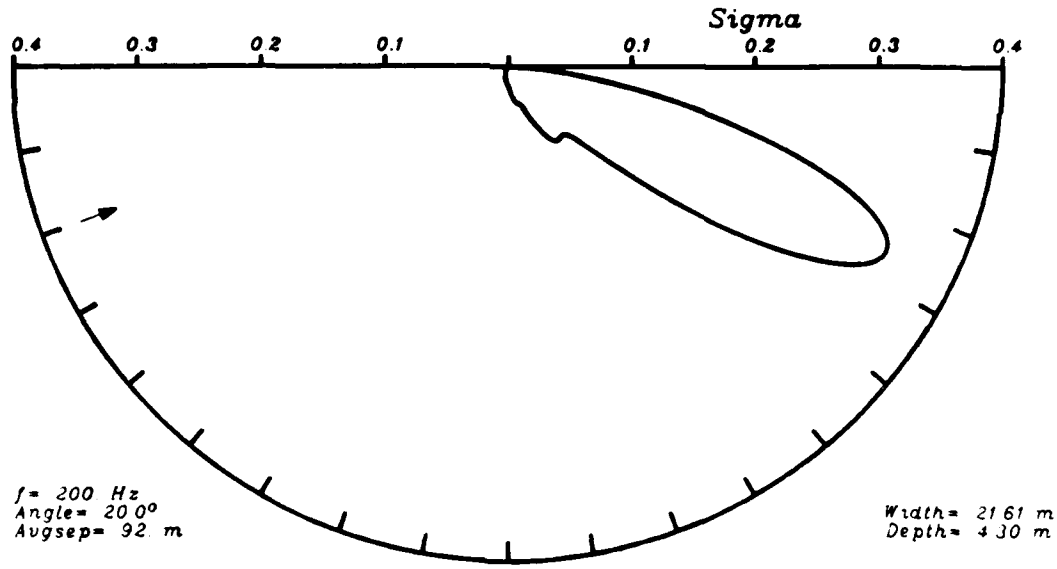

Figure 4.6. (Continued)

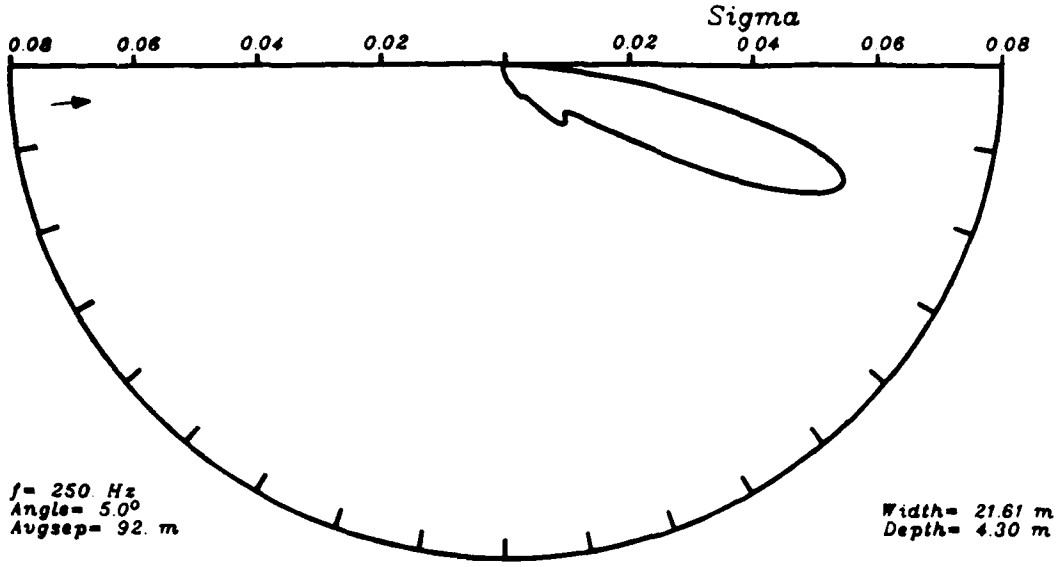

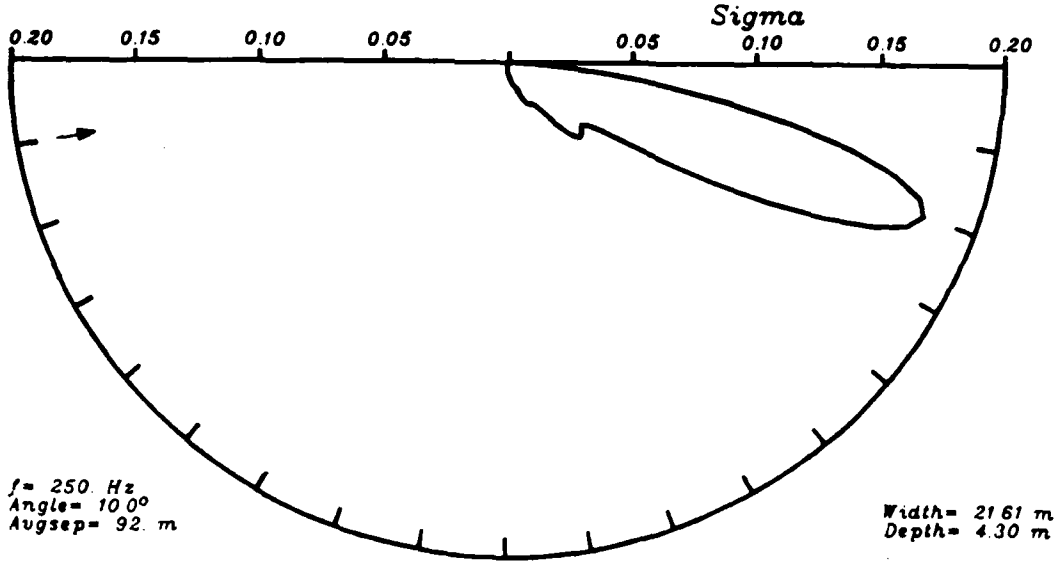

Figure 4.7. As in Figure 4.2, but at 250 Hz.

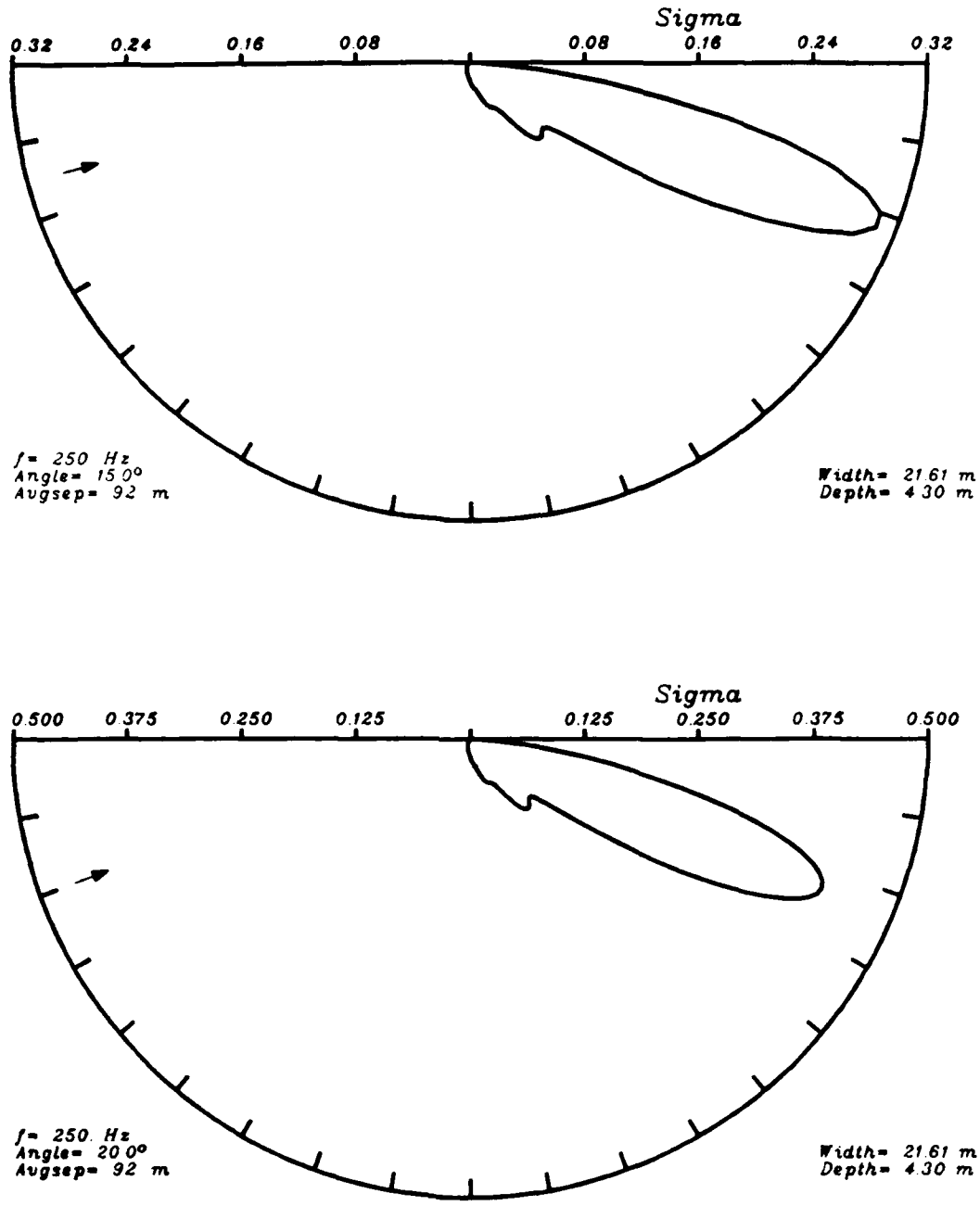

Figure 4.7. (Continued)

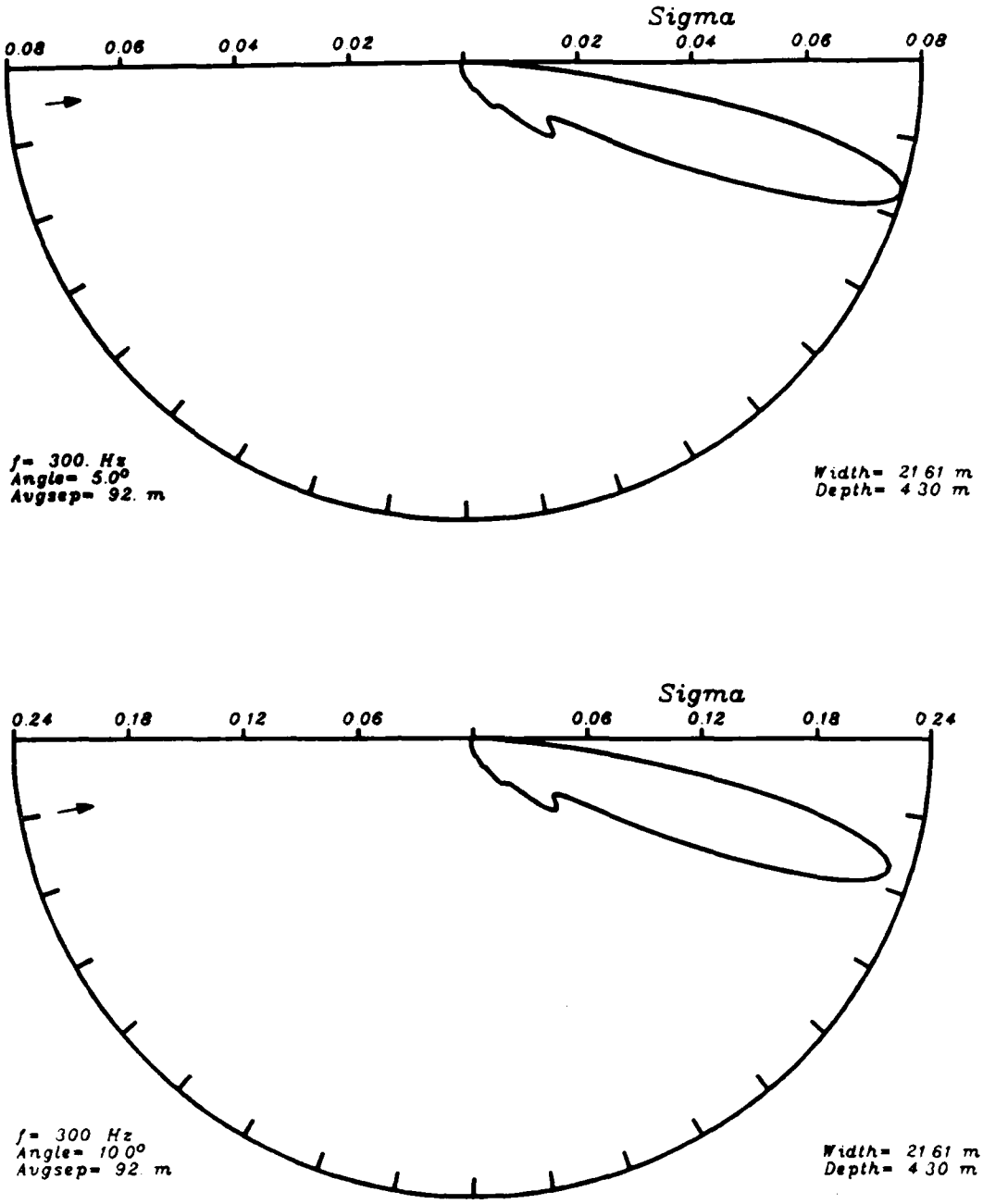

Figure 4.8. As in Figure 4.2, but at 300 Hz.

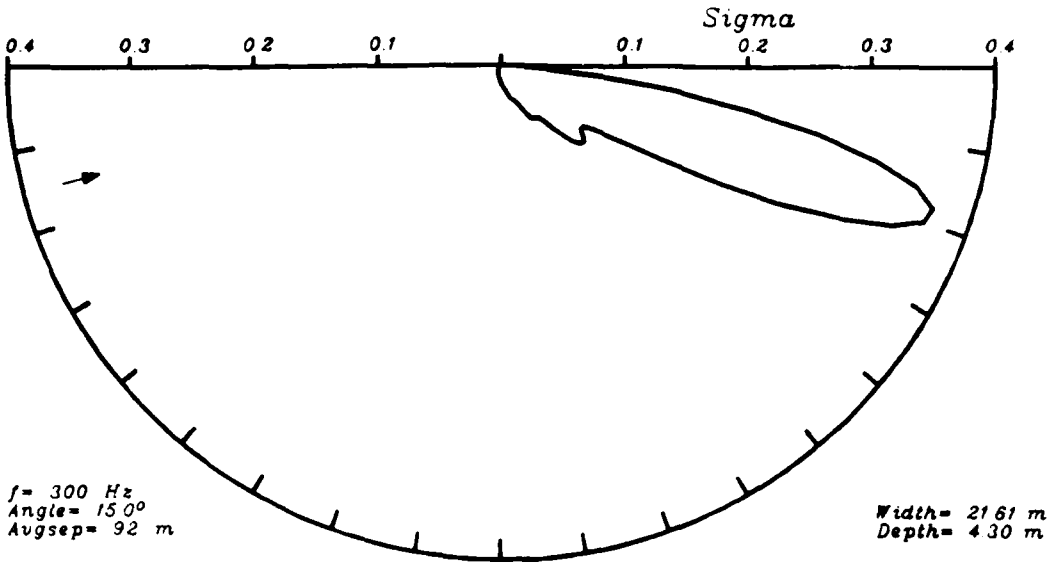

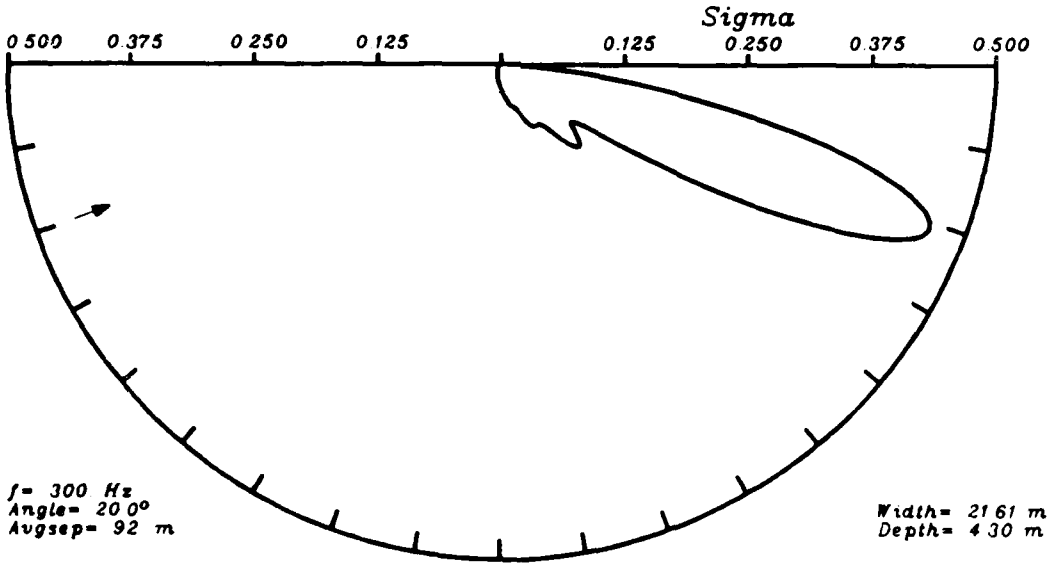

Figure 4.8. (Continued)

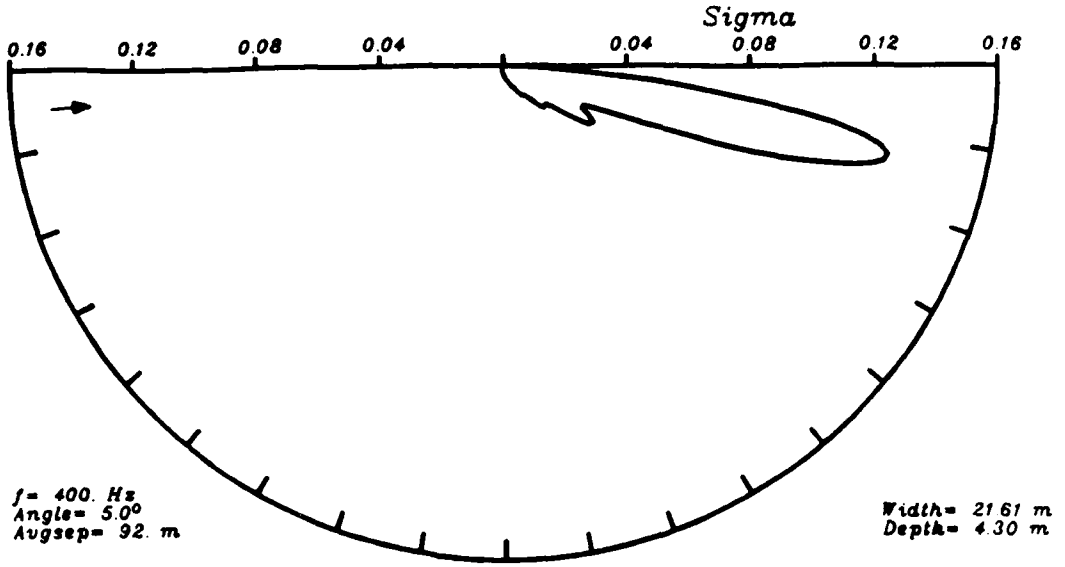

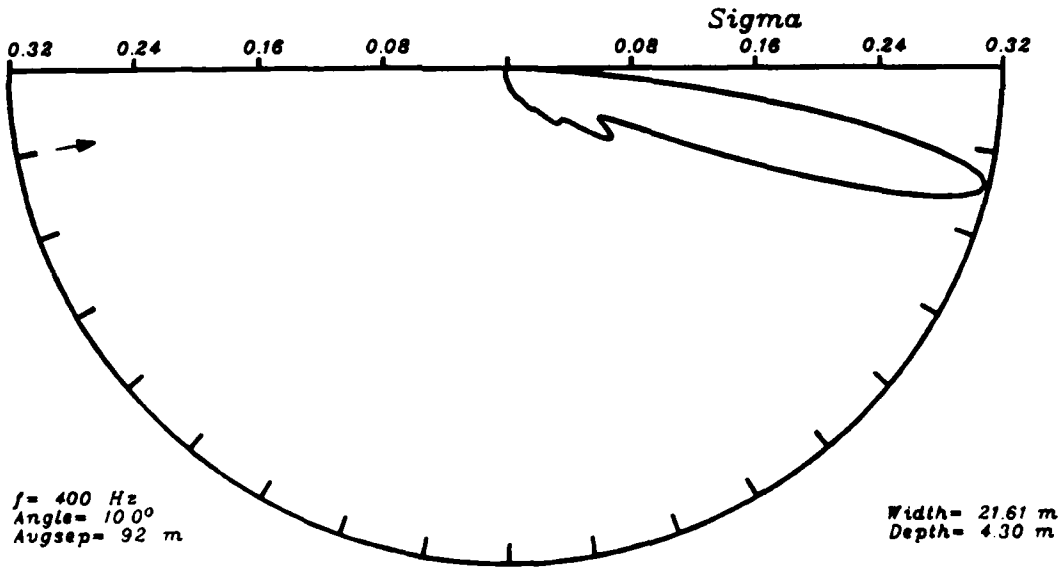

Figure 4.9. As in Figure 4.2, but at 400 Hz.

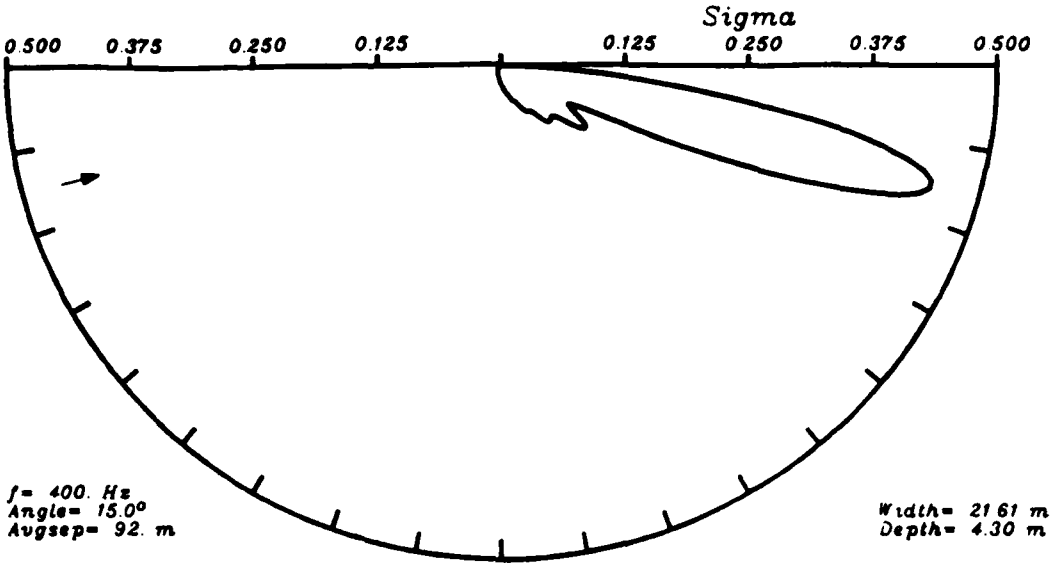

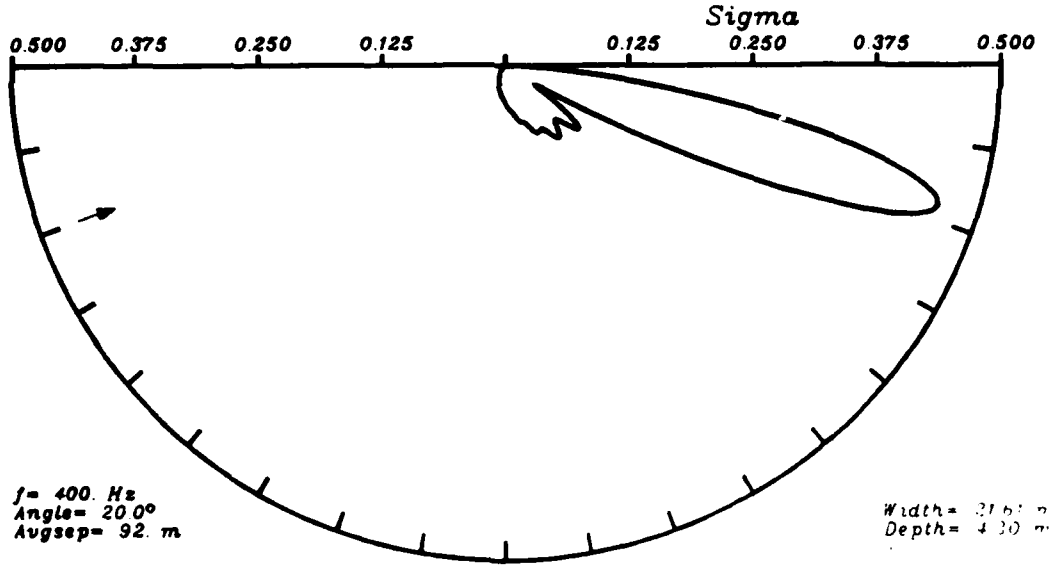

Figure 4.9. (Continued)

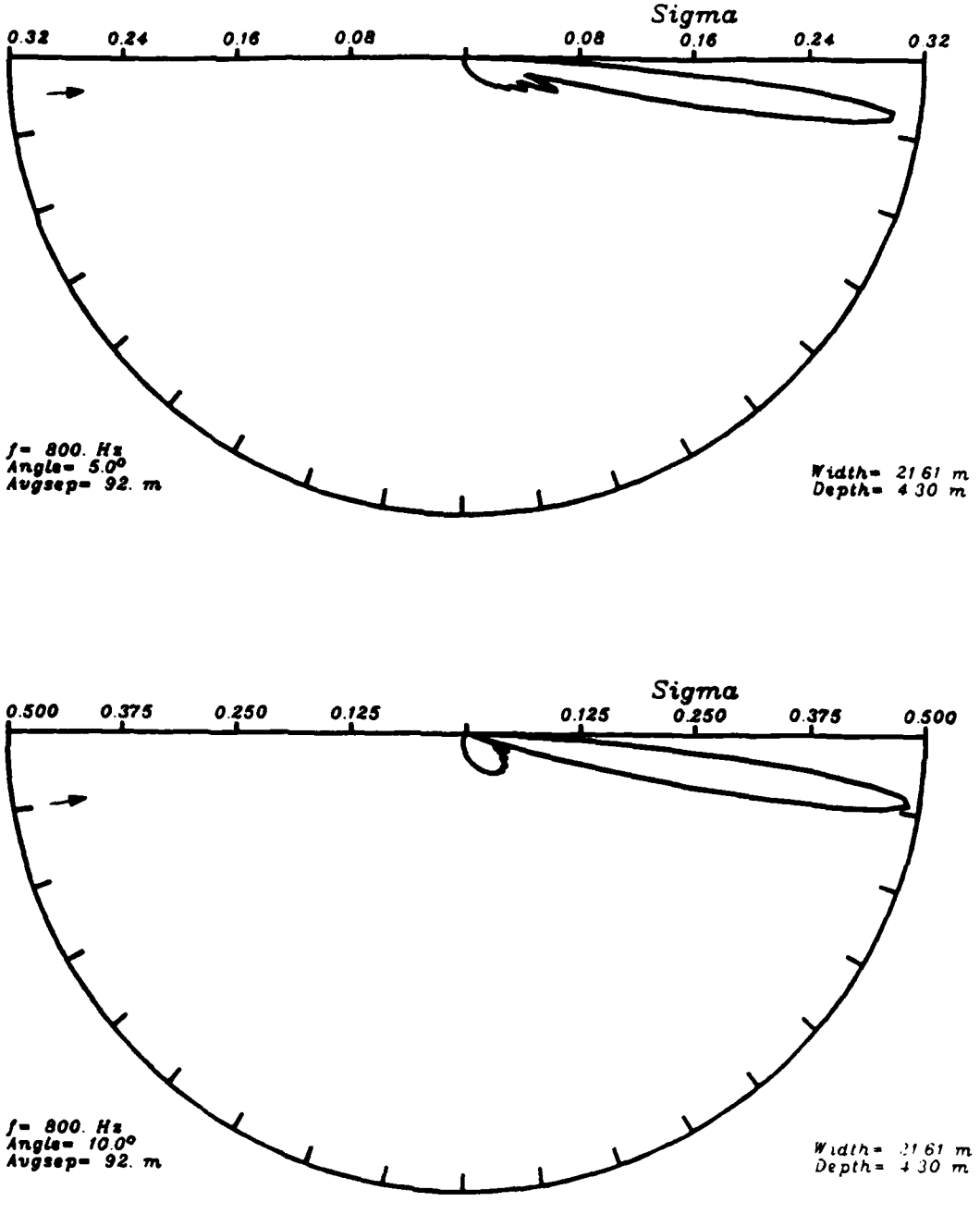

Figure 4.10. As in Figure 4.2, but at 800 Hz.

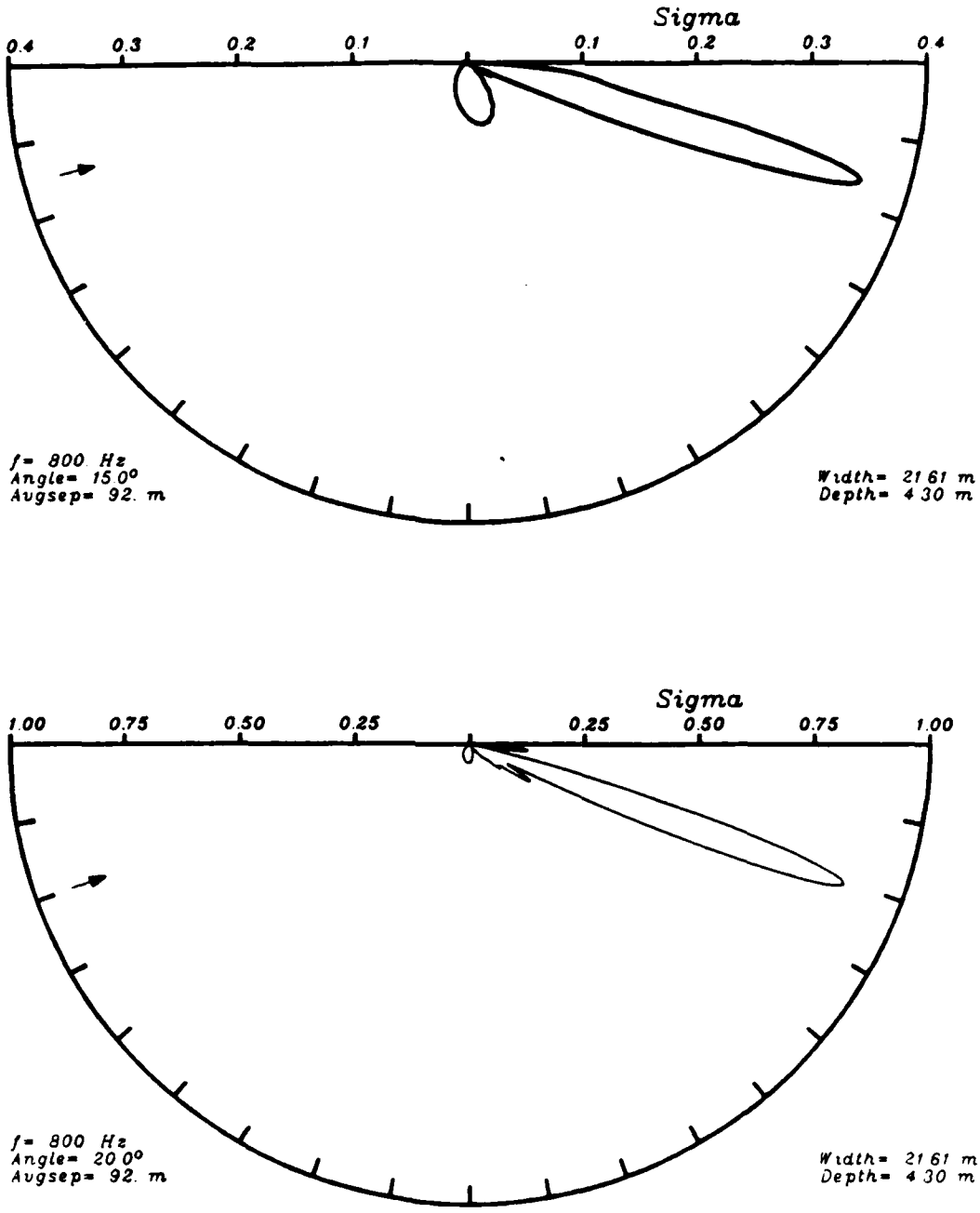

Figure 4.10. (Continued)

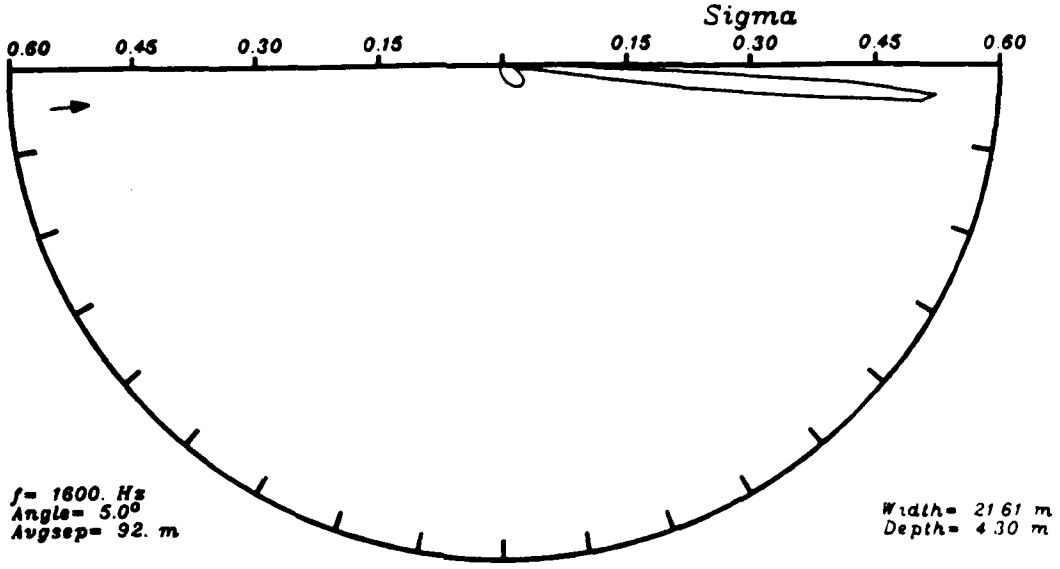

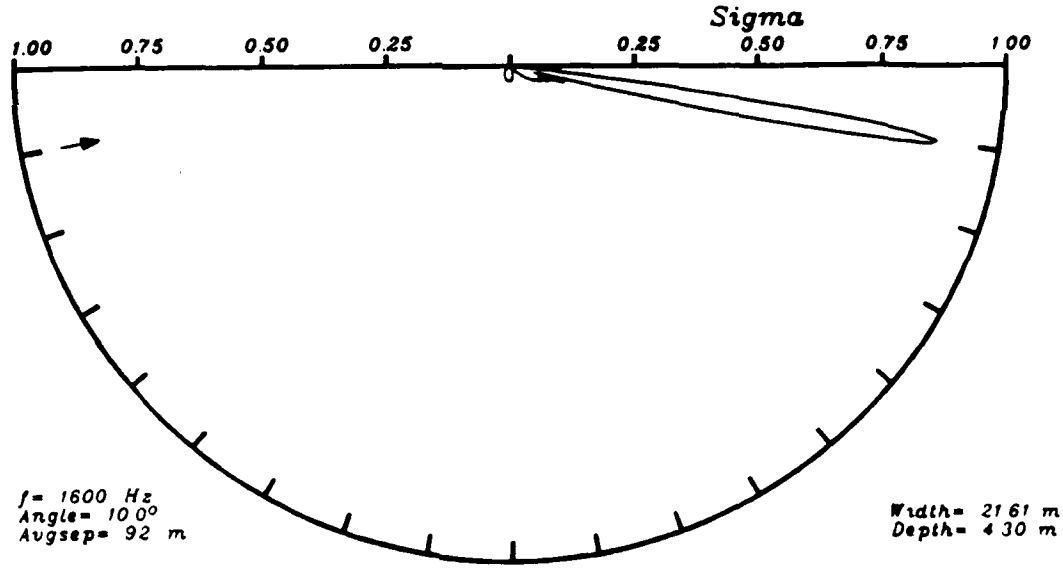

Figure 4.11. As in Figure 4.2, but at 1600 Hz.

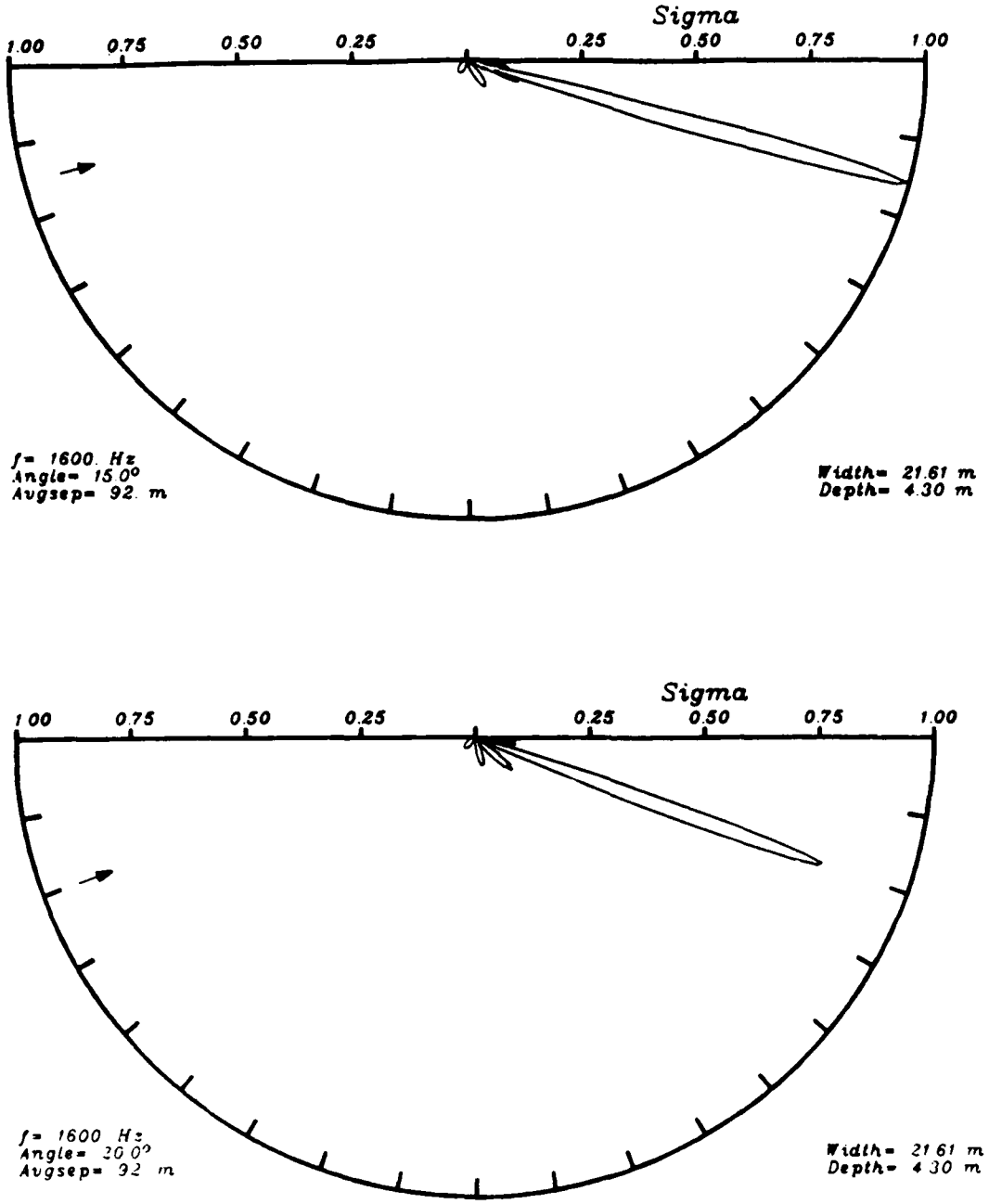

Figure 4.11. (Continued)

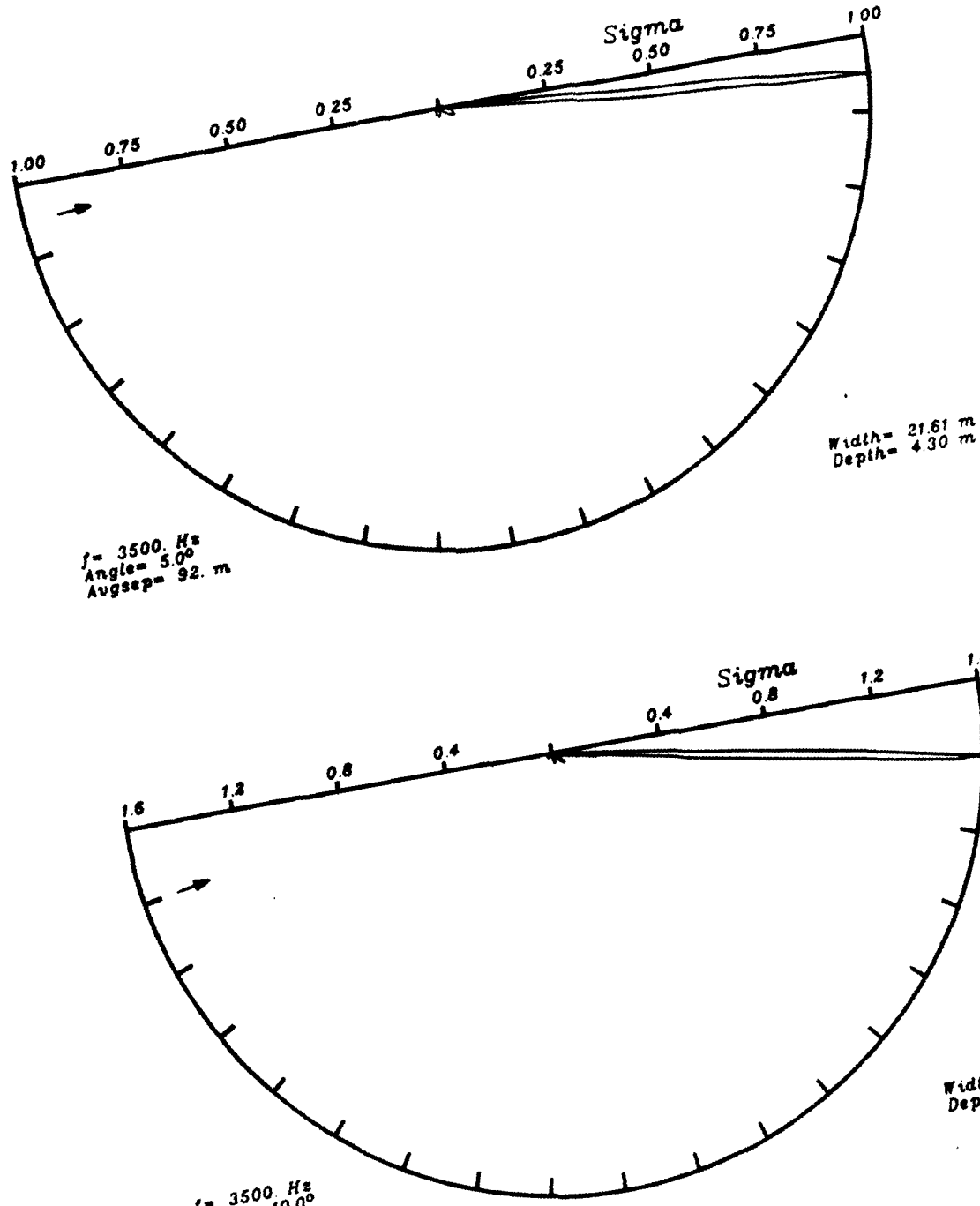

Figure 4.12. As in Figure 4.2, but at 3500 Hz.

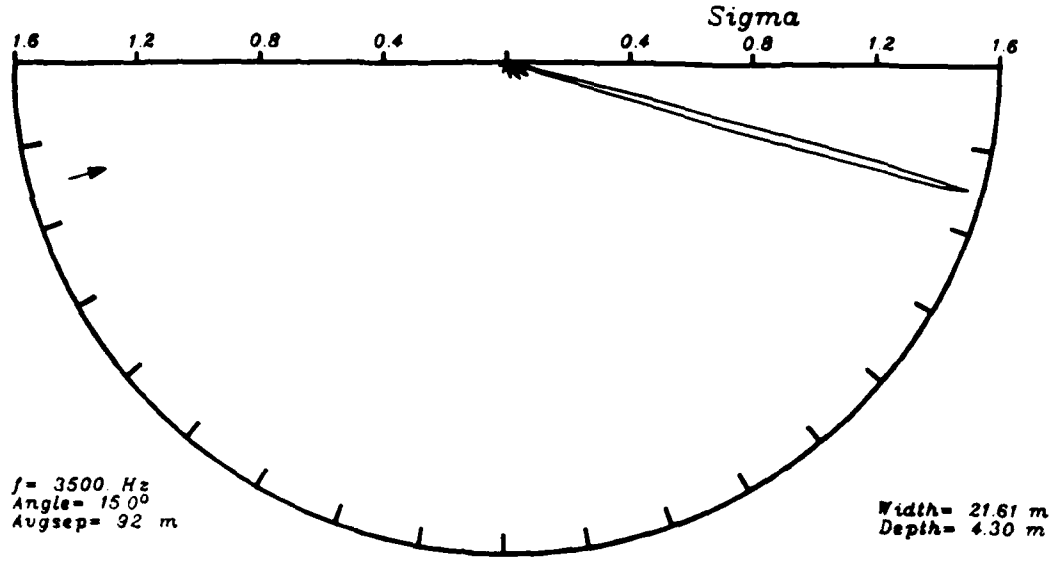

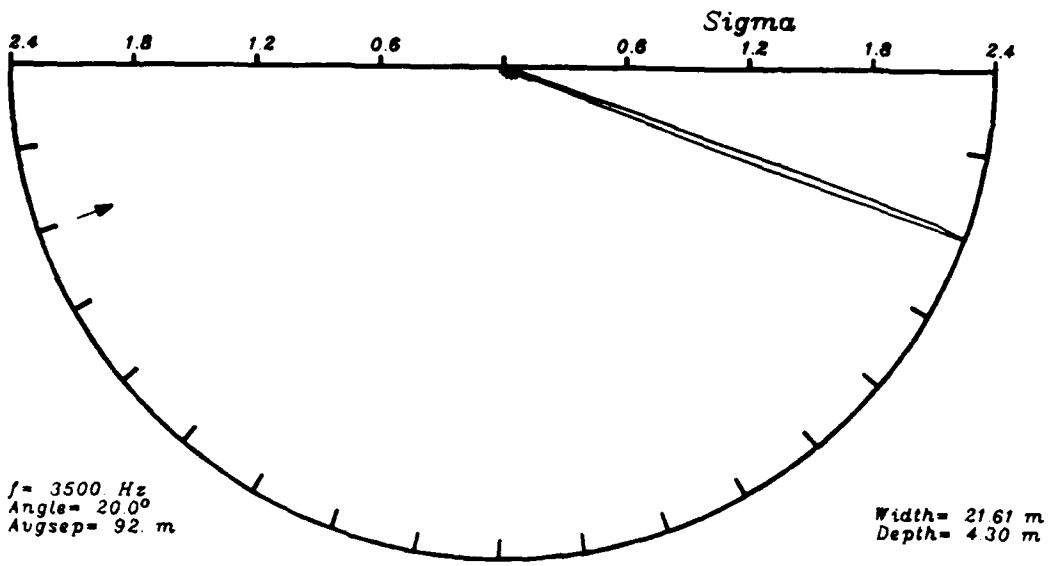

Figure 4.12. (Continued)

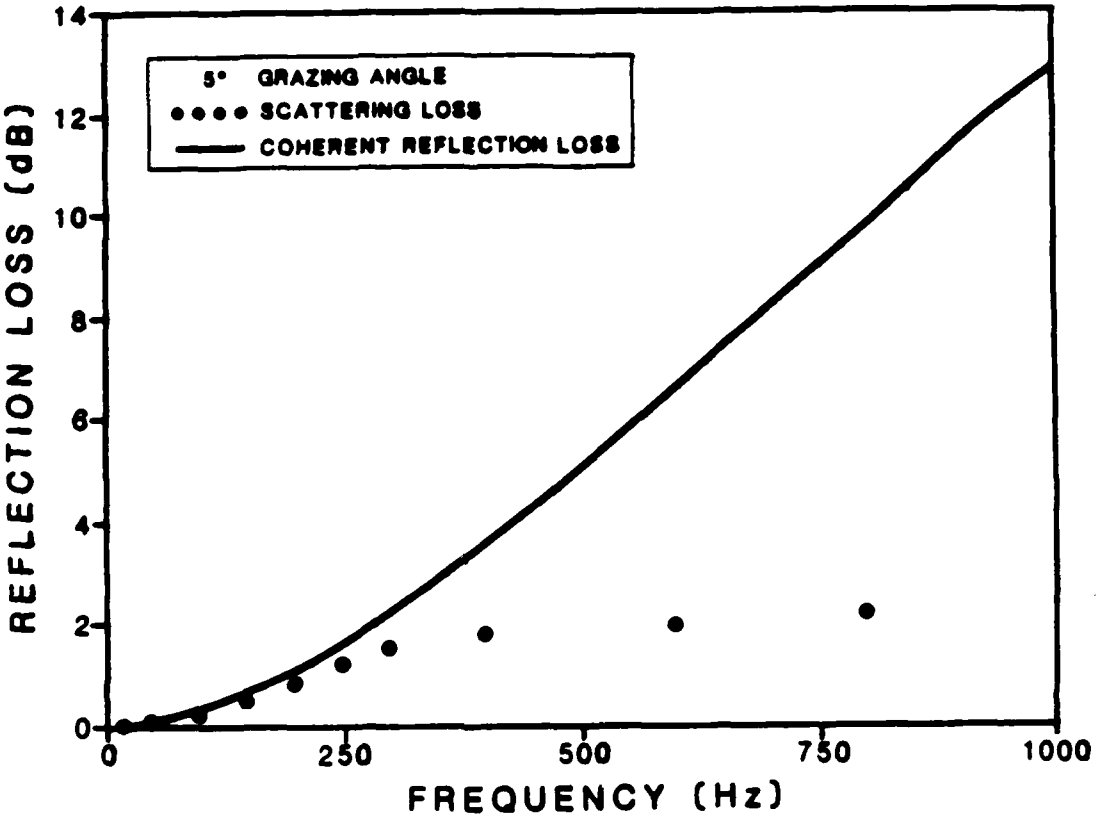

Figure 4.13. Reflection coefficient R (solid curve) and 1-SL (symbols) for 5° grazing angle. The quantity 1-SL (SL is scattering loss) represents the sum of coherent energy plus the propagating component of incoherent scattering energy.

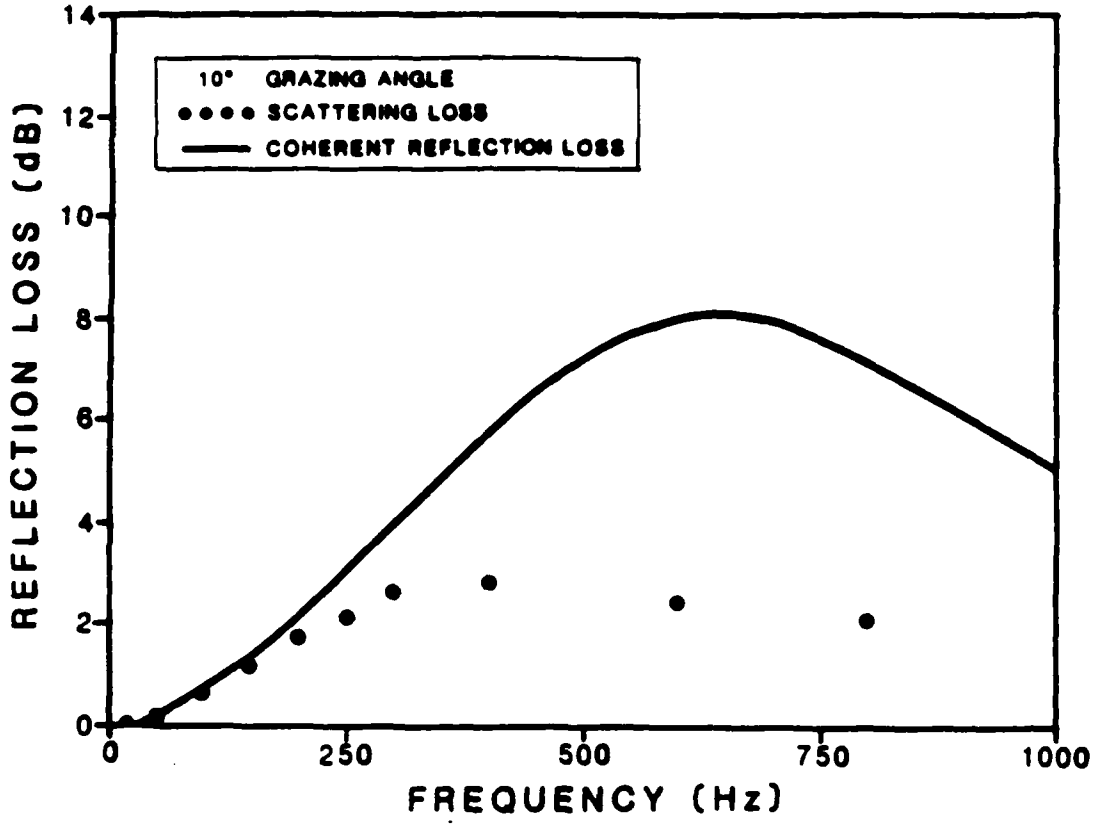

Figure 4.14. Reflection coefficient R (solid curve) and 1-SL (symbols) for 10° grazing angle. The quantity 1-SL (SL is scattering loss) represents the sum of coherent energy plus the propagating component of incoherent scattering energy.

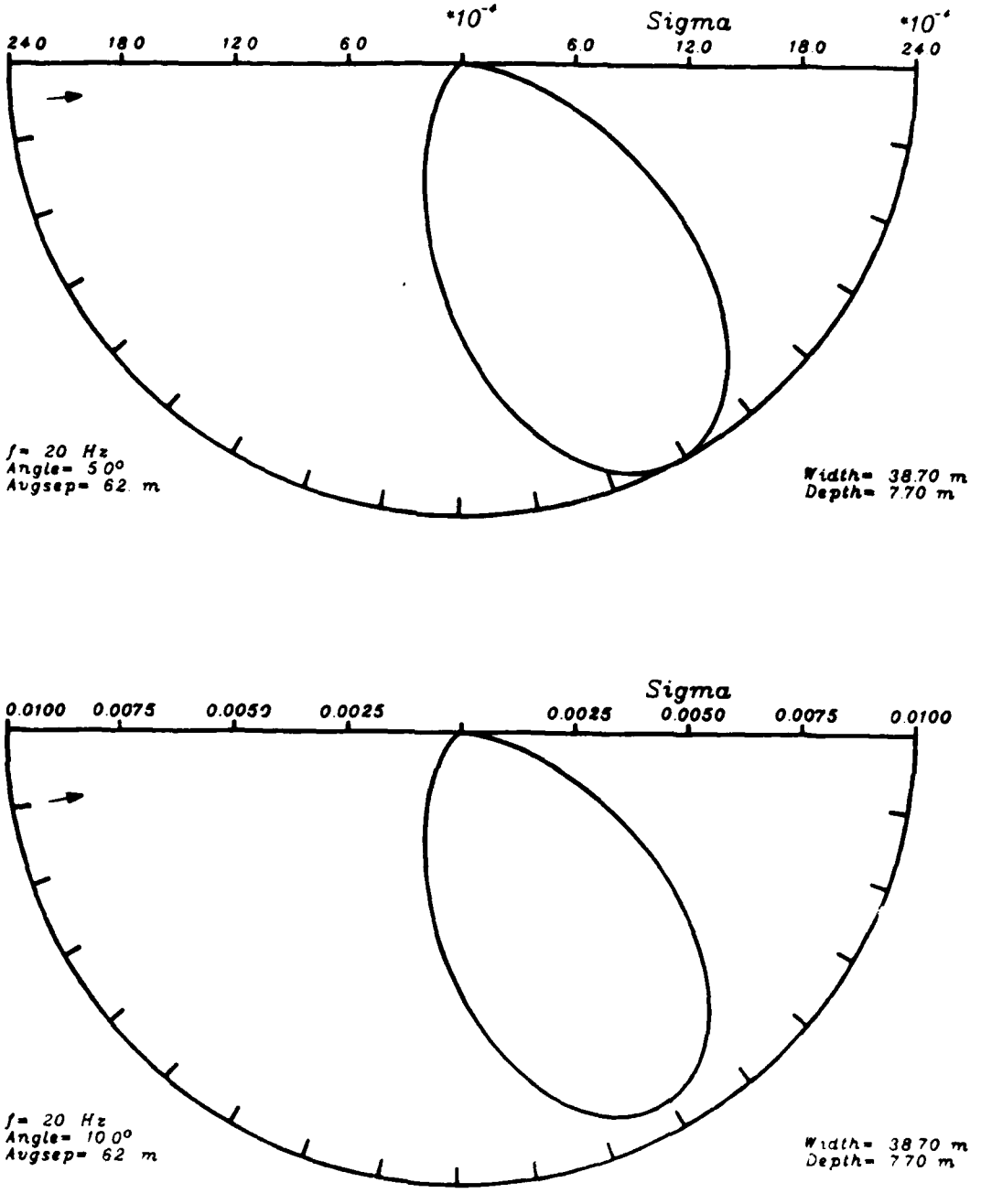

Figure 4.15. Scattering cross sections at 20 Hz. Incoming grazing angles are 5°, 10°, 15°, and 20°. Keel parameters: Width = 38.7 m, Depth = 7.7 m, Average Separation = 62 m.

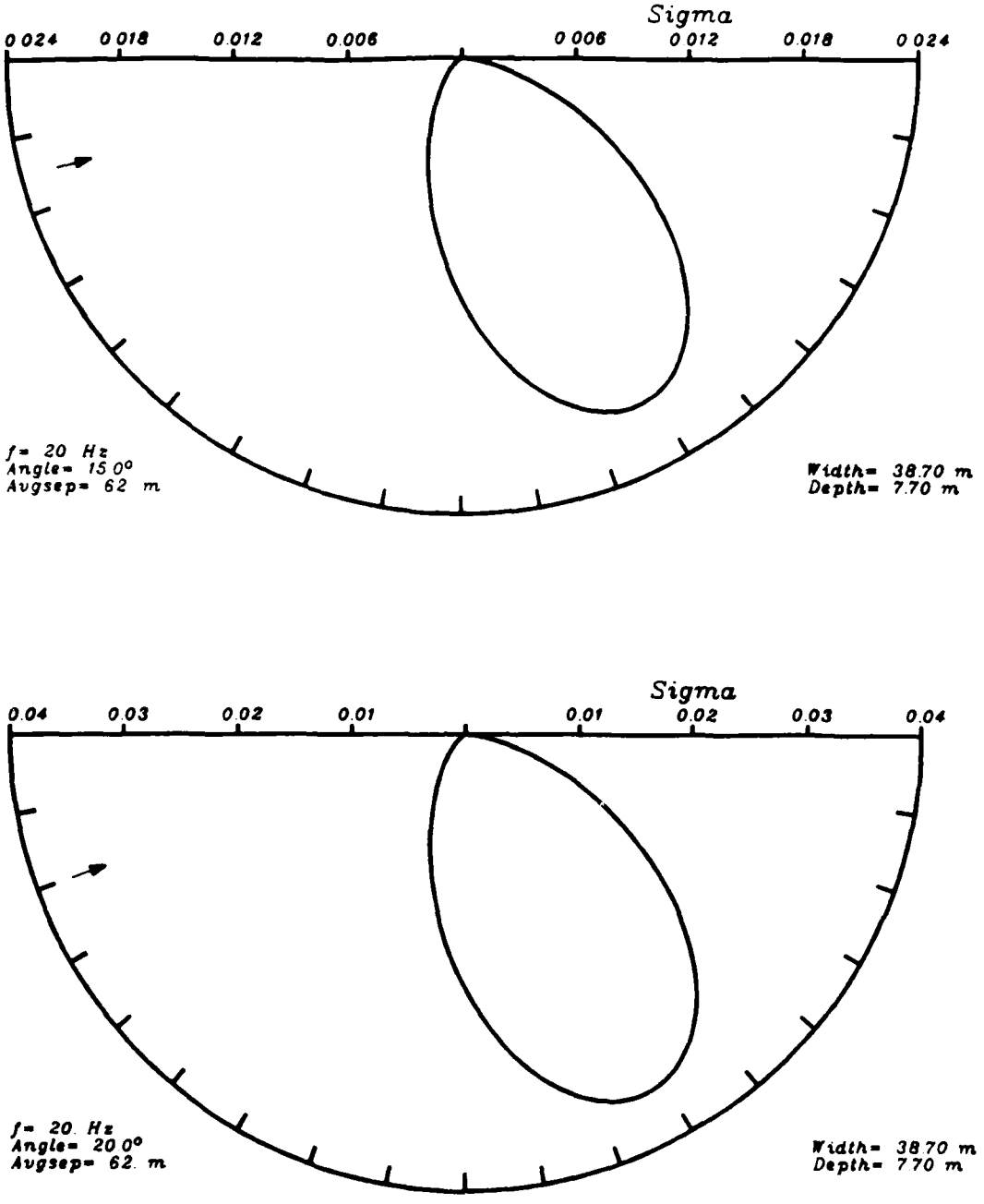

Figure 4.15. (Continued)

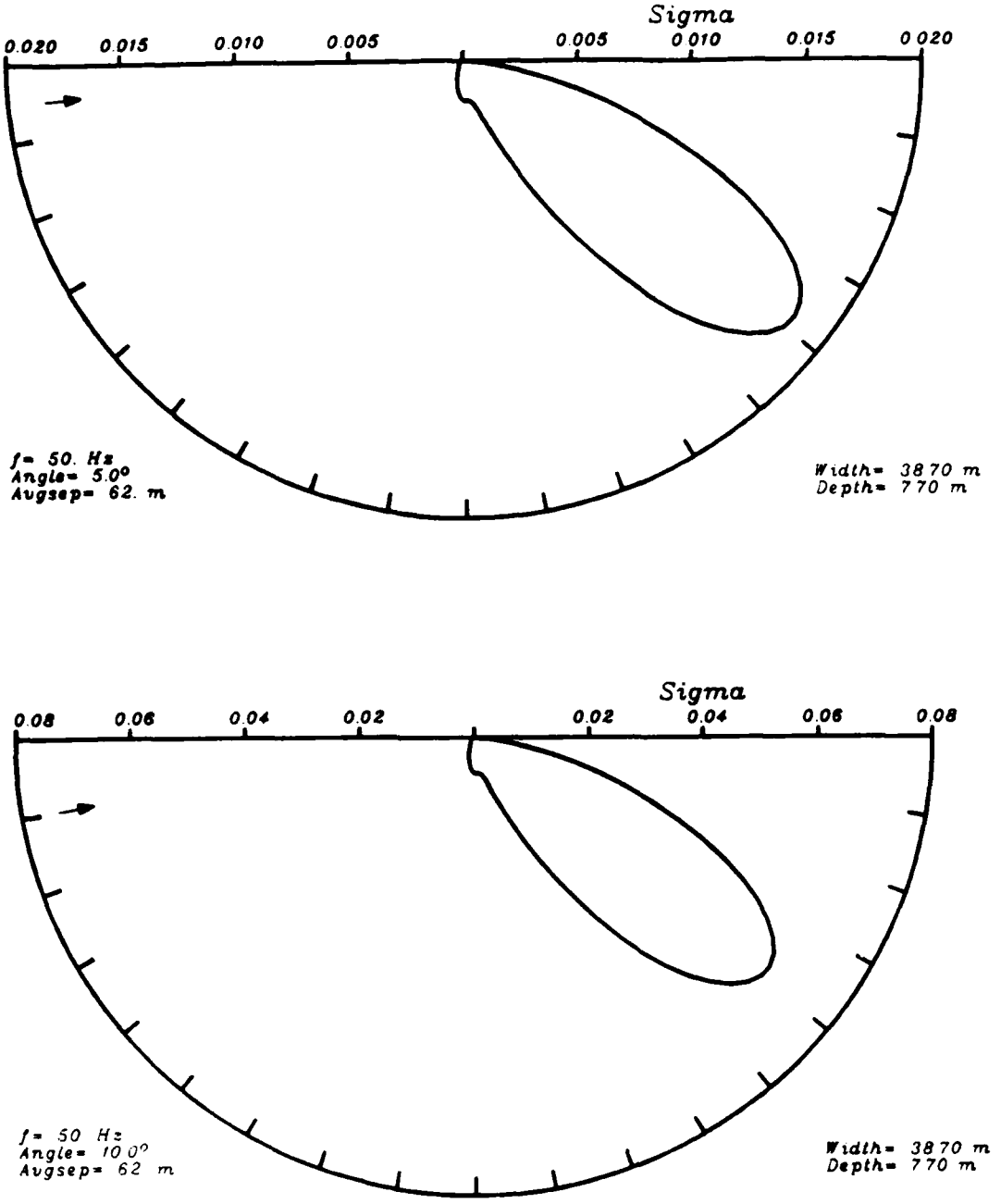

Figure 4.16. As in Figure 4.15, but at 50 Hz.

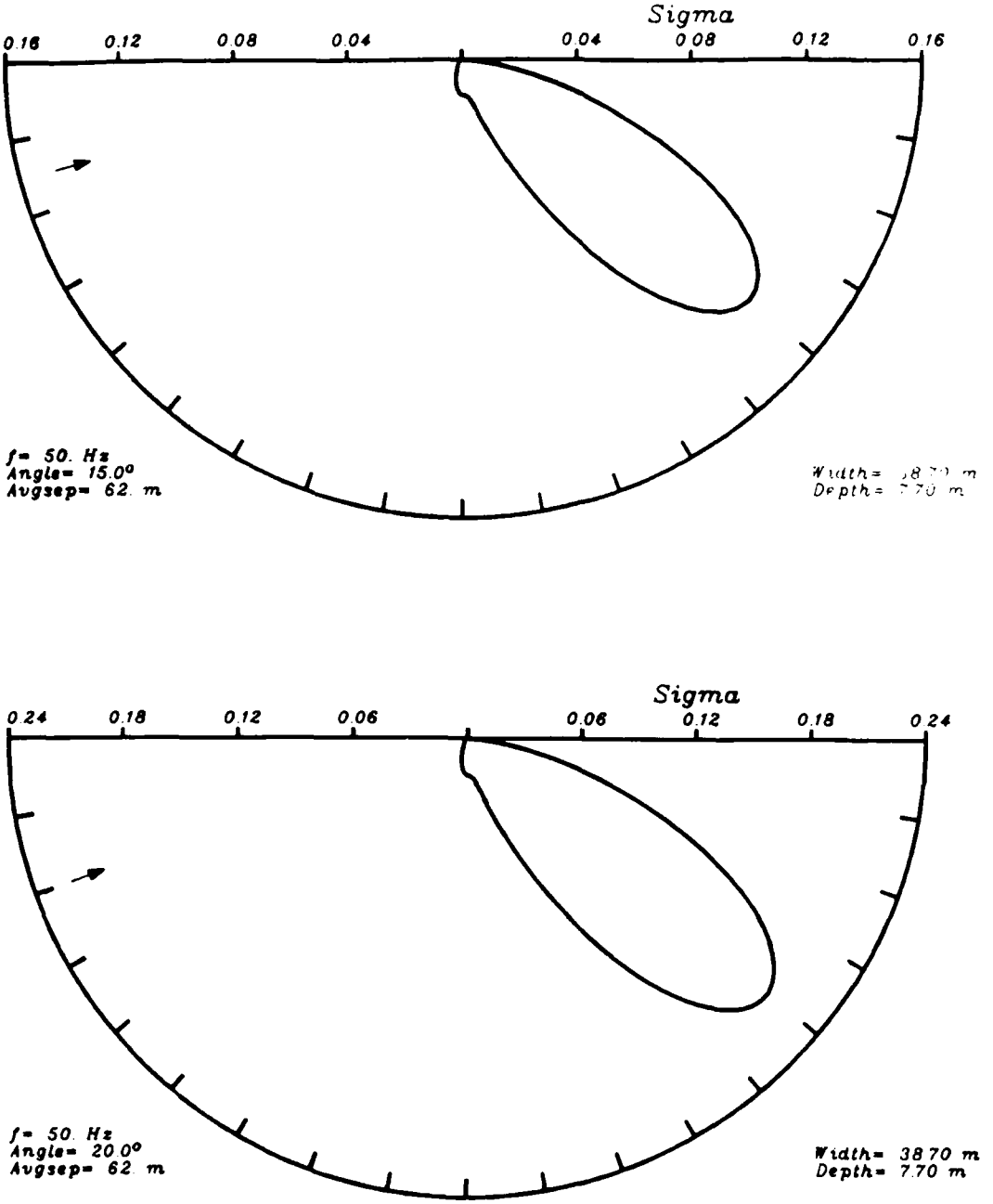

Figure 4.16. (Continued)

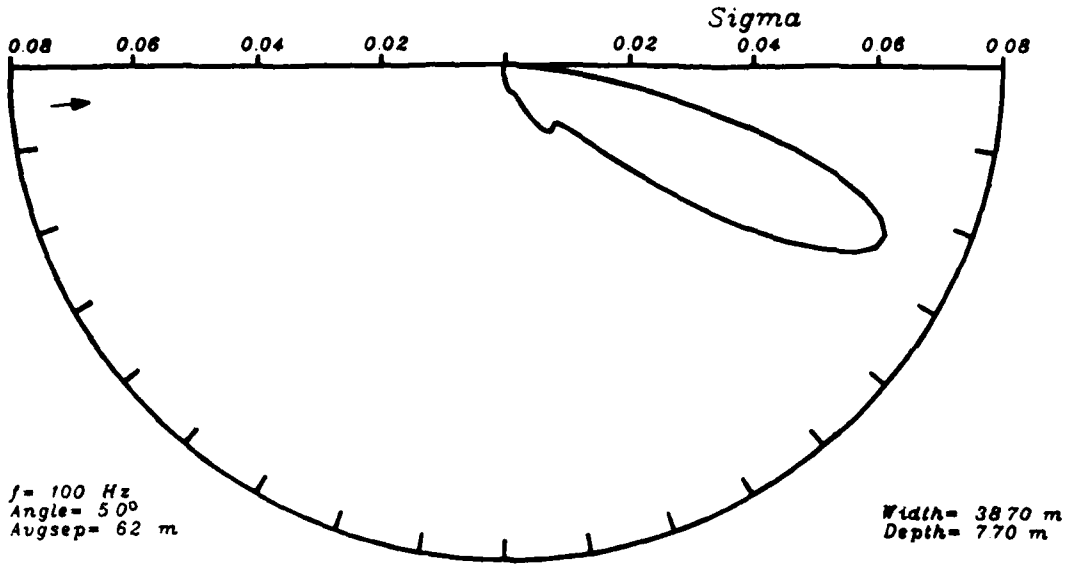

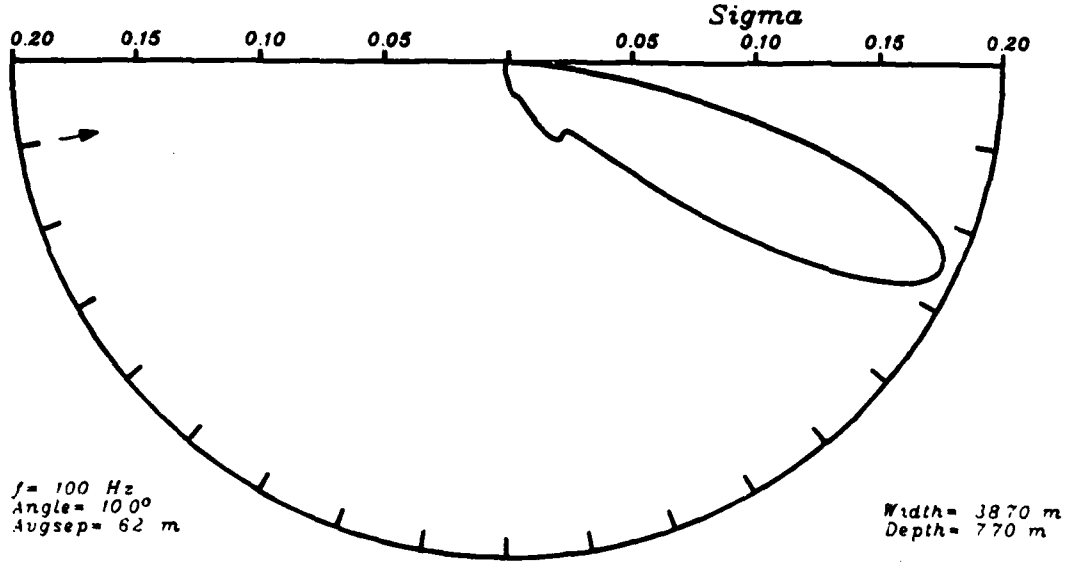

Figure 4.17. As in Figure 4.15, but at 100 Hz.

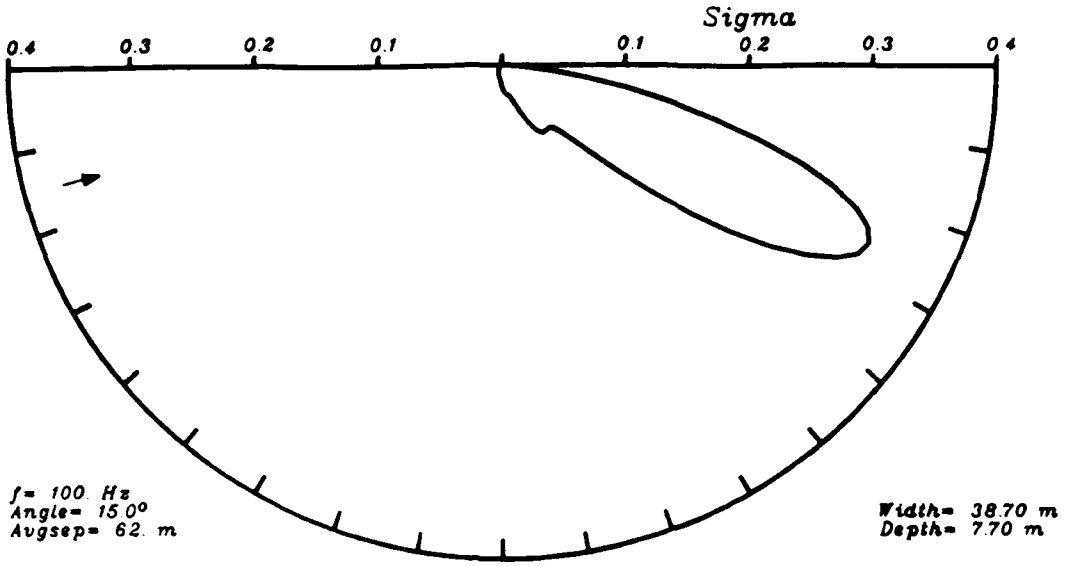

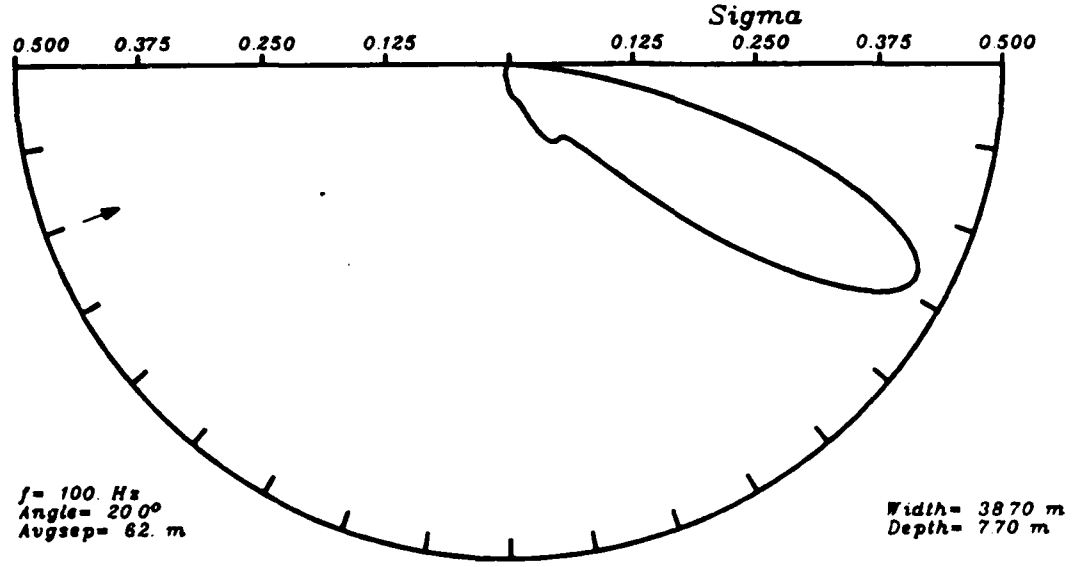

Figure 4.17. (Continued)

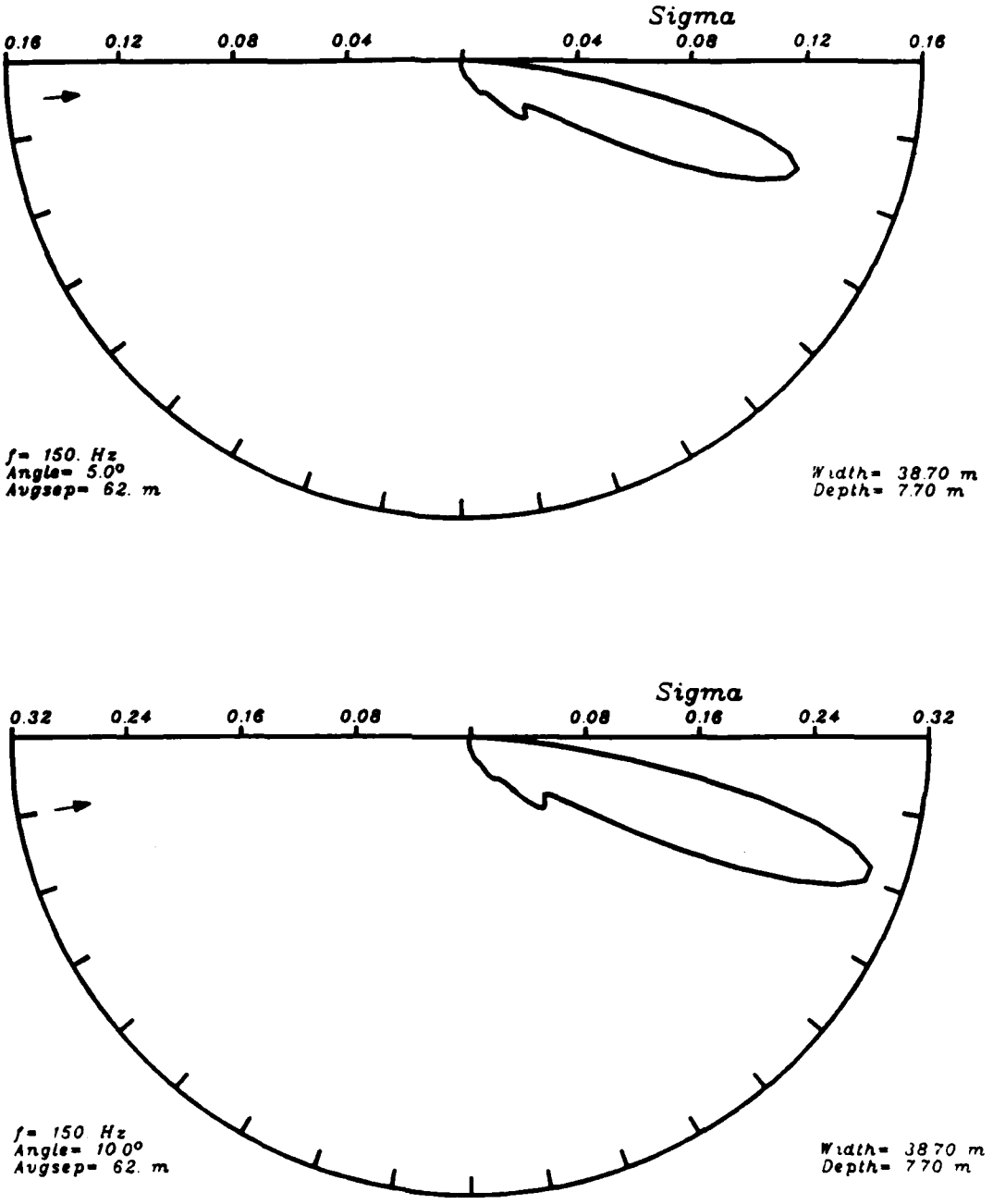

Figure 4.18. As in Figure 4.15, but at 150 Hz.

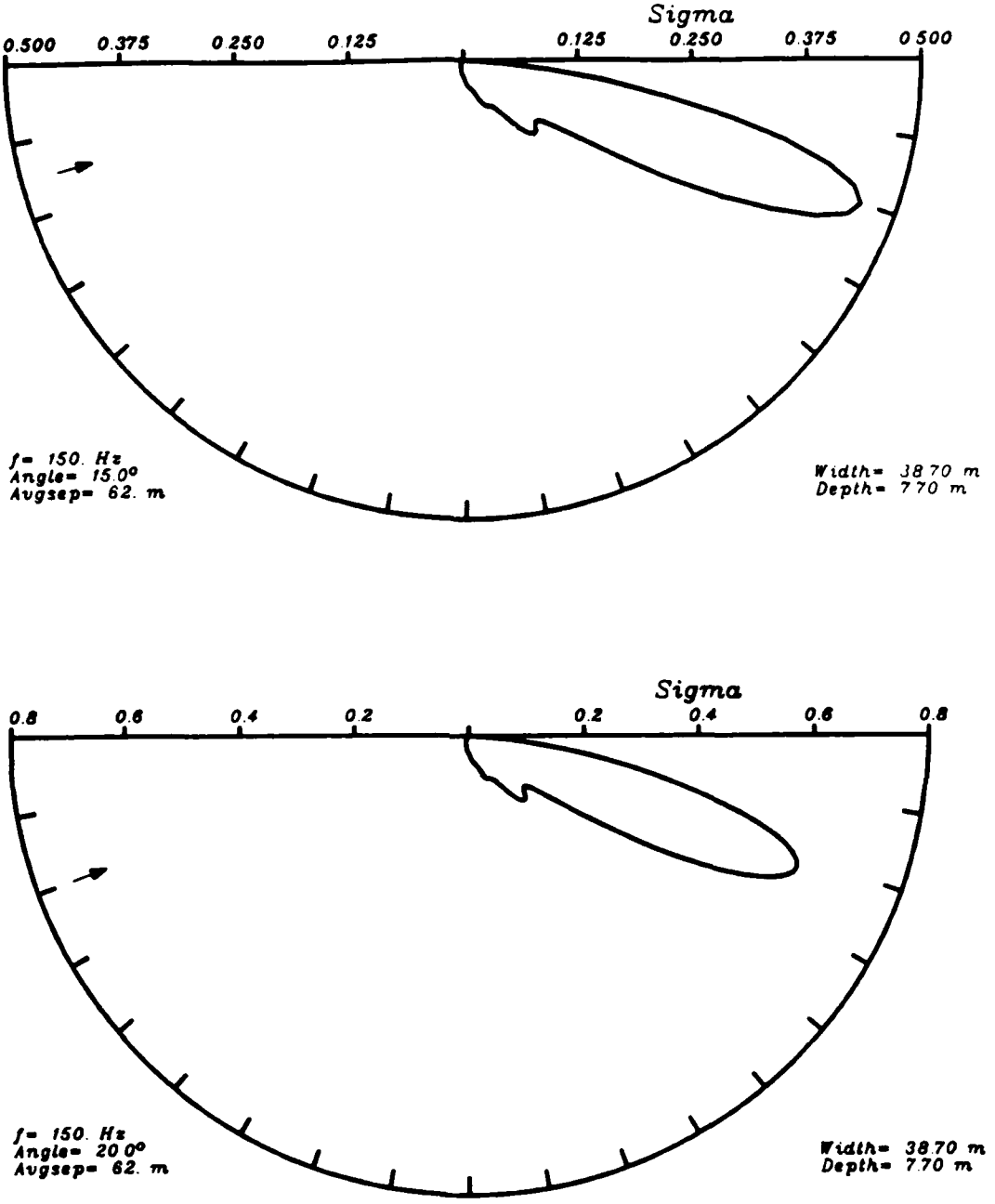

Figure 4.18. (Continued)

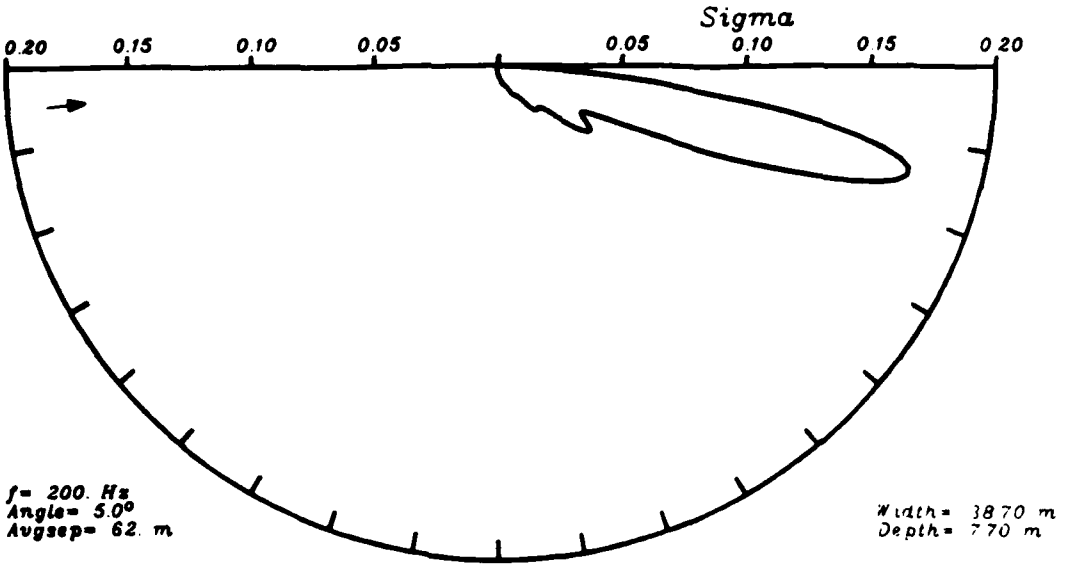

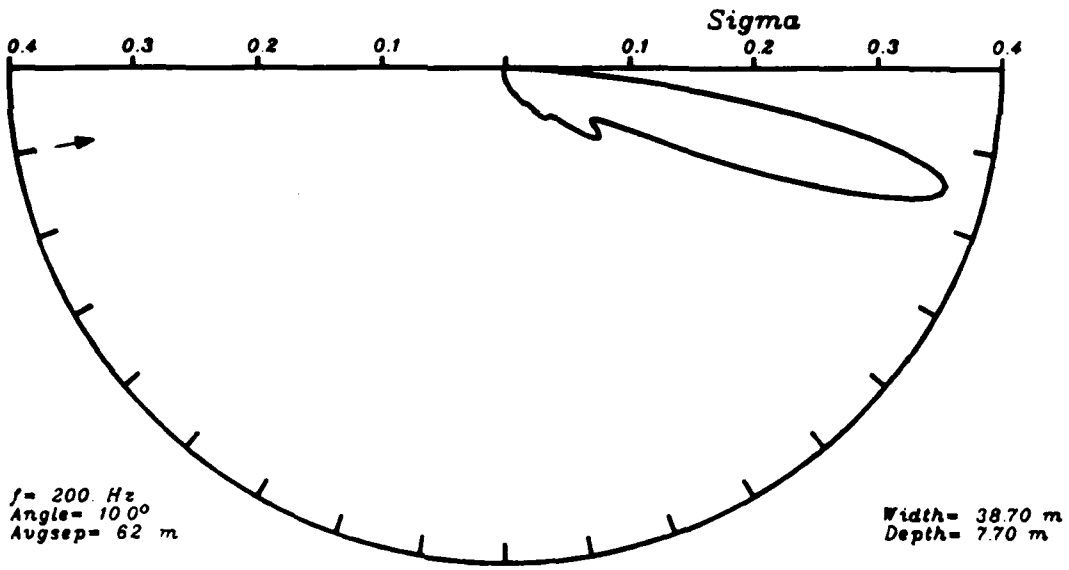

Figure 4.19. As in Figure 4.15, but at 200 Hz.

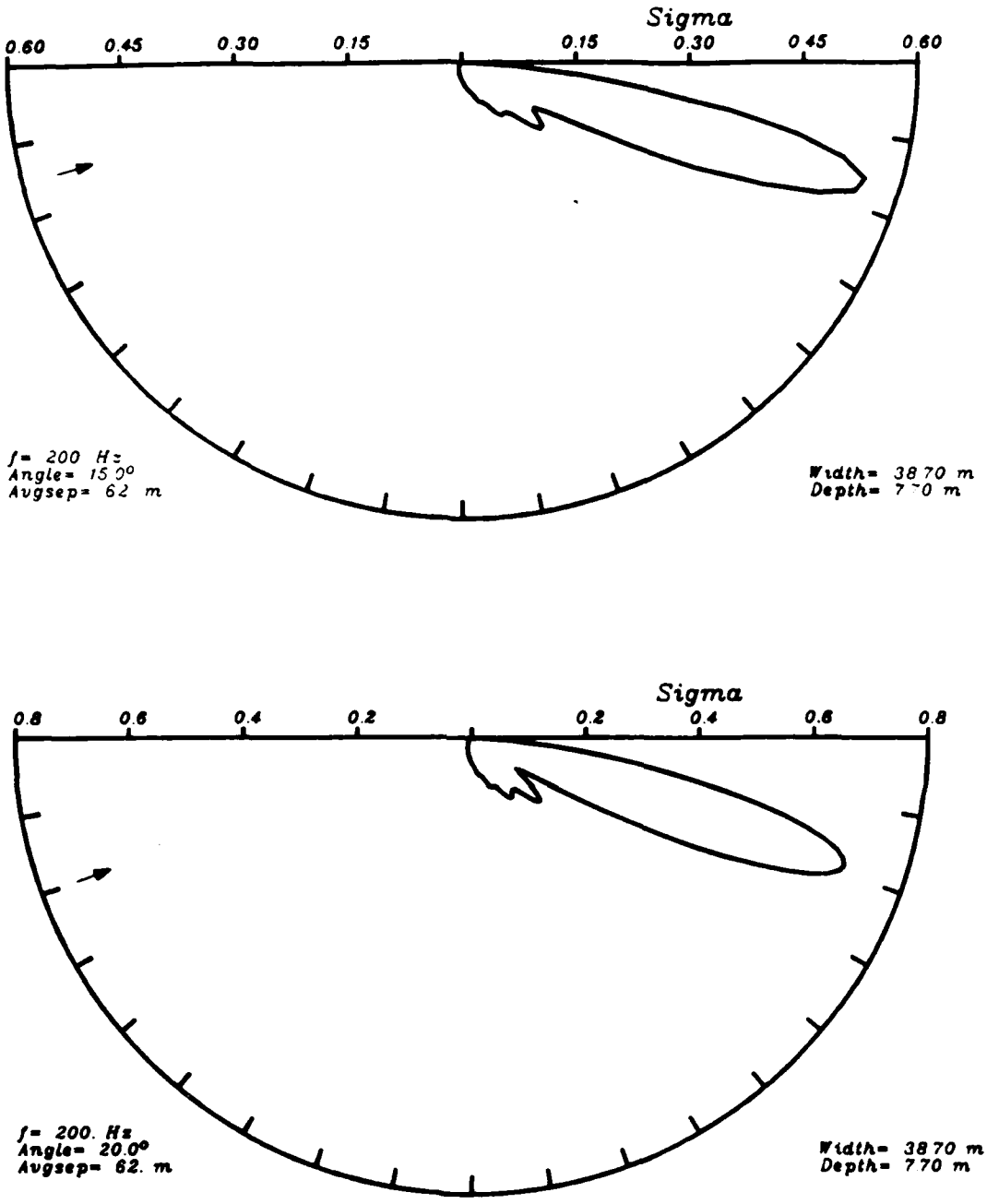

Figure 4.19. (Continued)

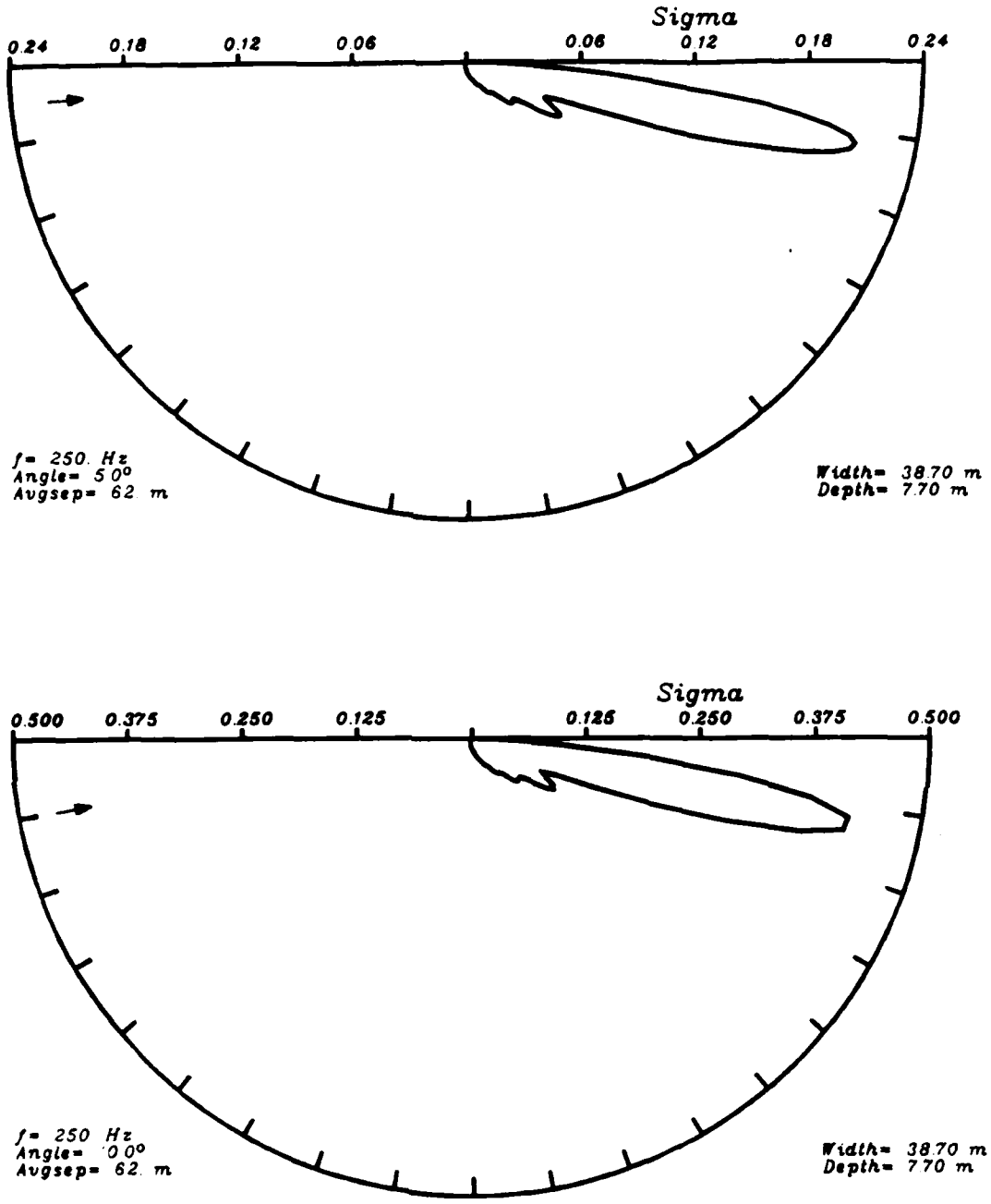

Figure 4.20. As in Figure 4.15, but at 250 Hz.

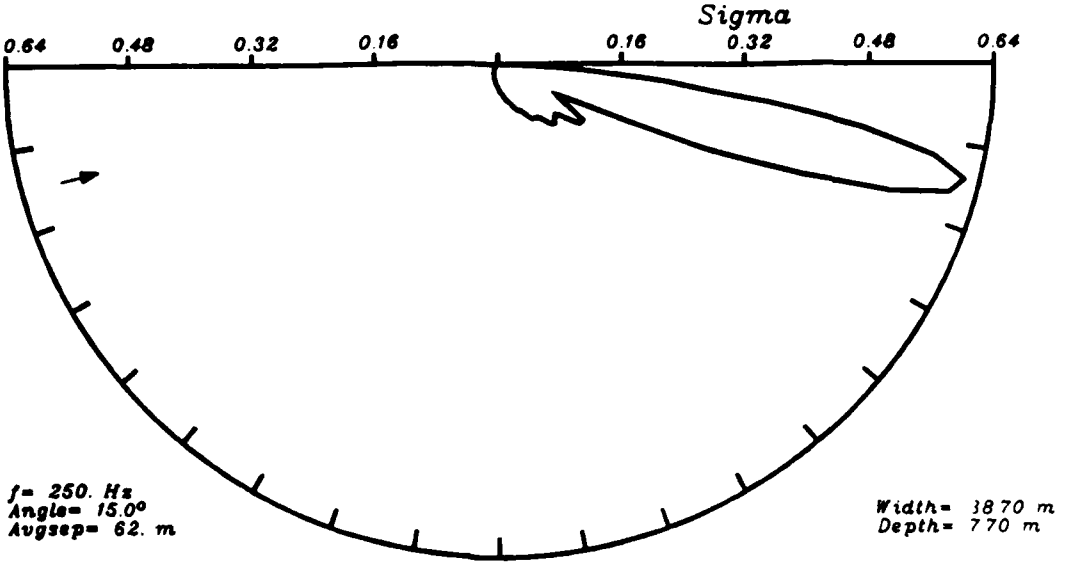

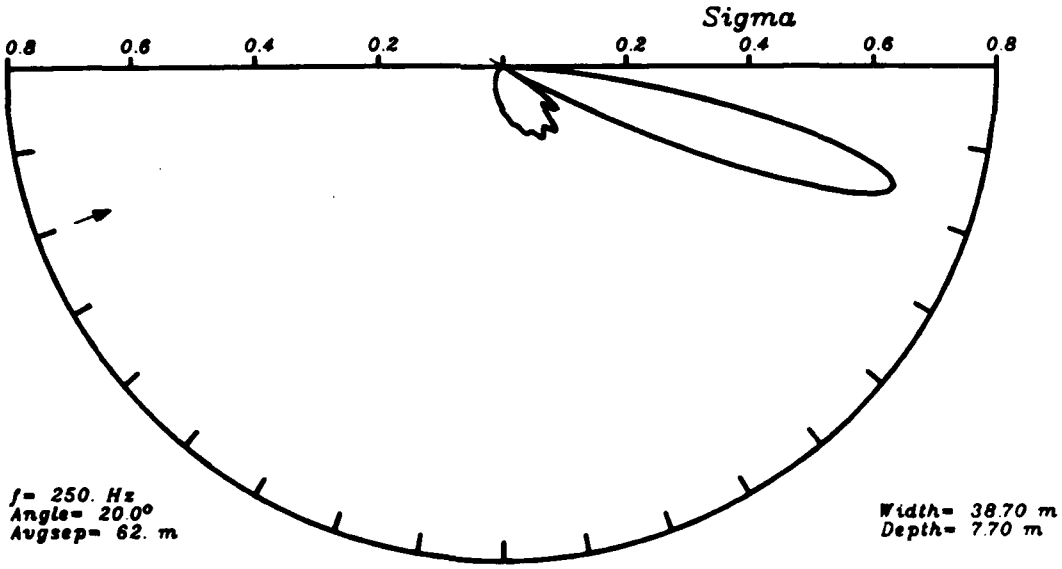

Figure 4.20. (Continued)

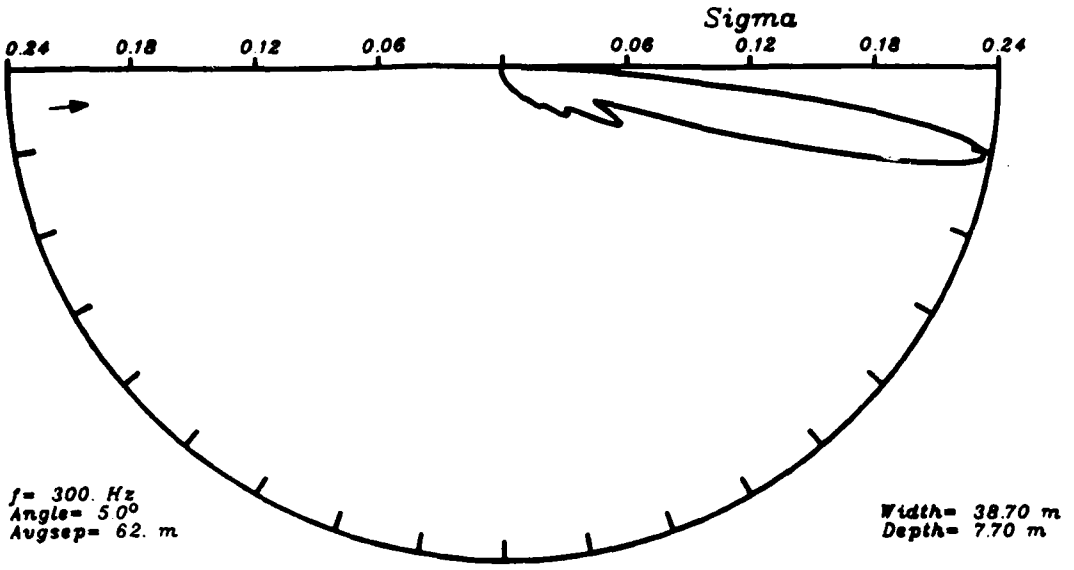

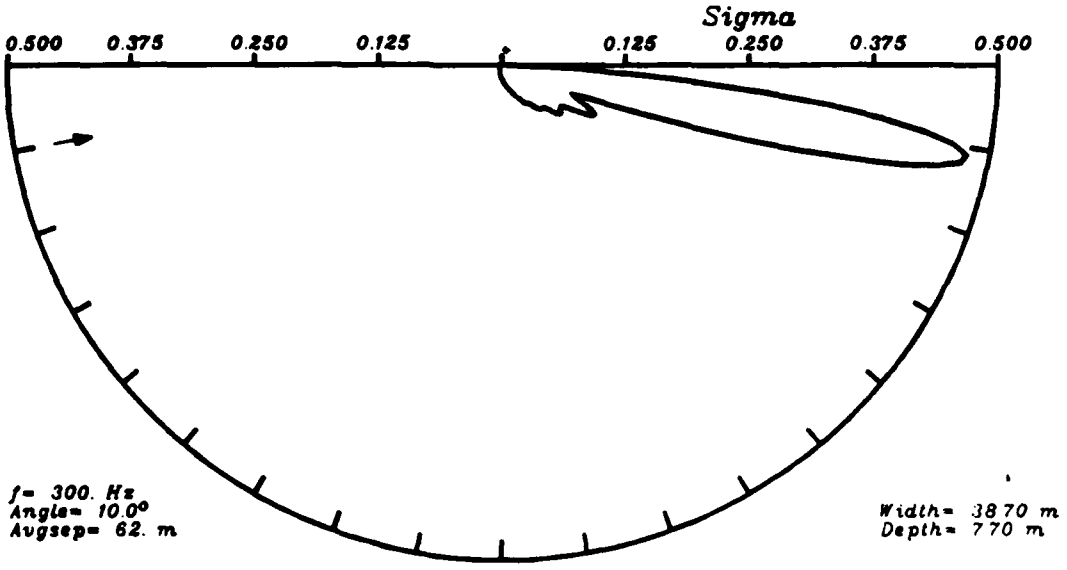

Figure 4.21. As in Figure 4.15, but at 300 Hz.

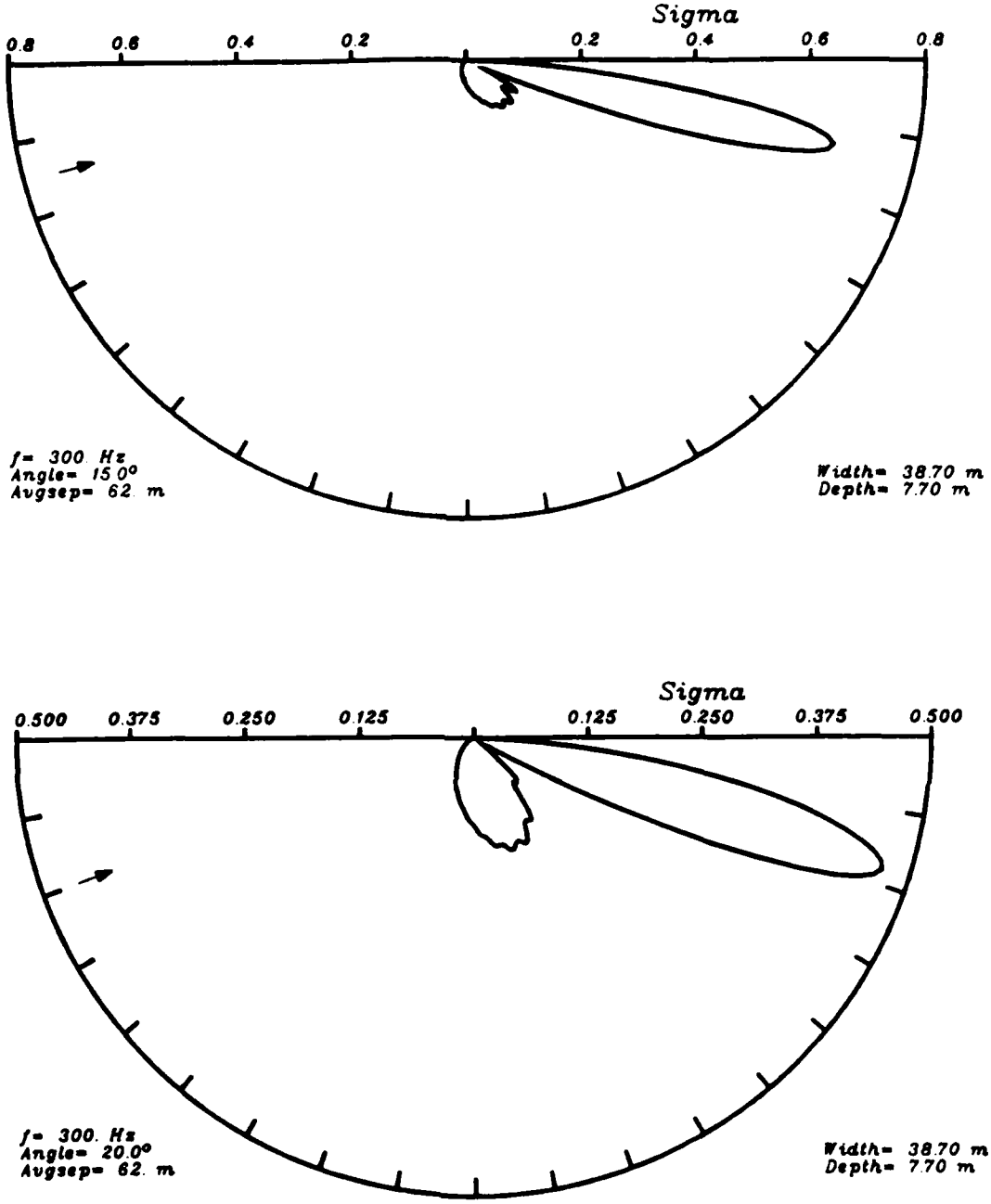

Figure 4.21. (Continued)

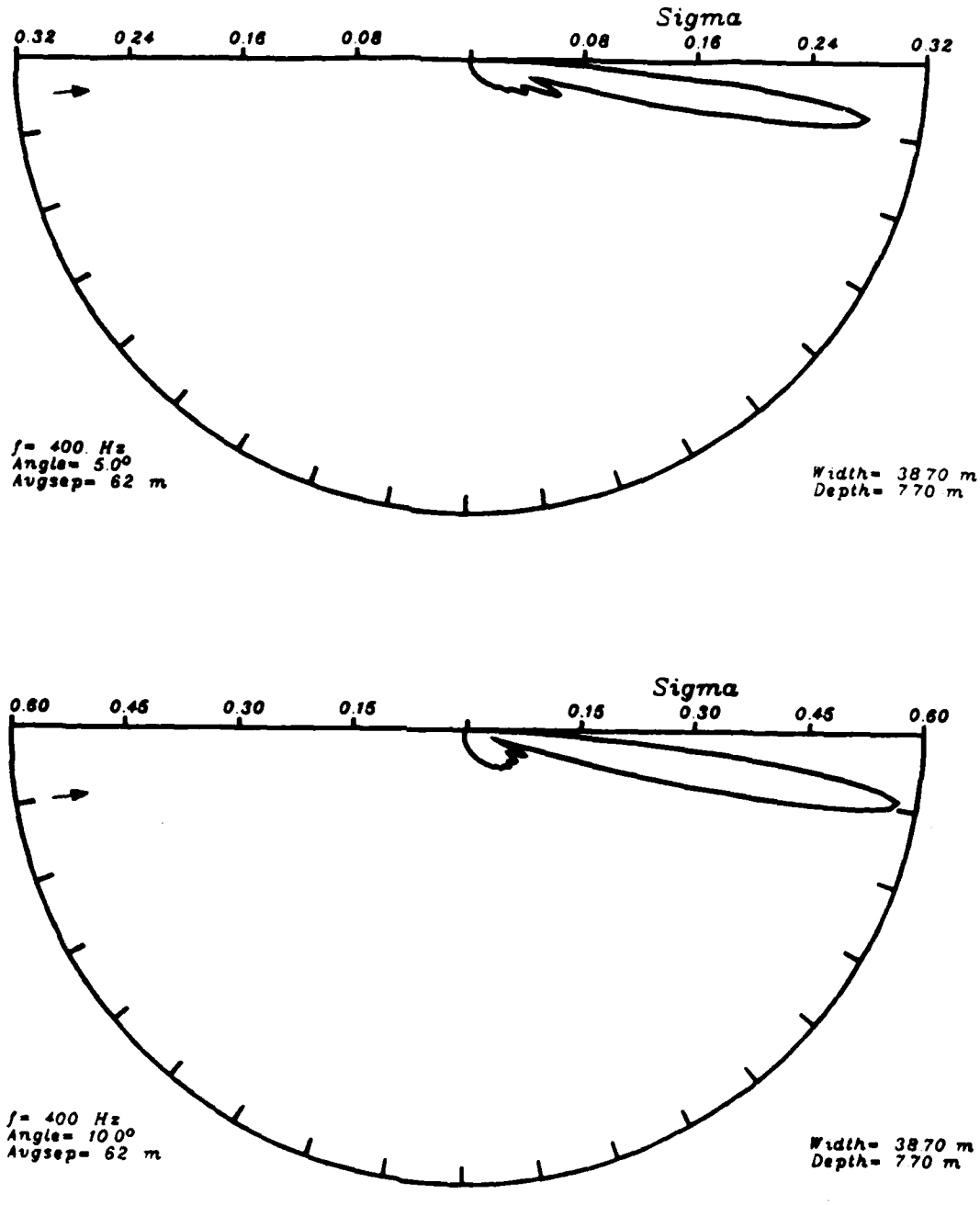

Figure 4.22. As in Figure 4.15, but at 400 Hz.

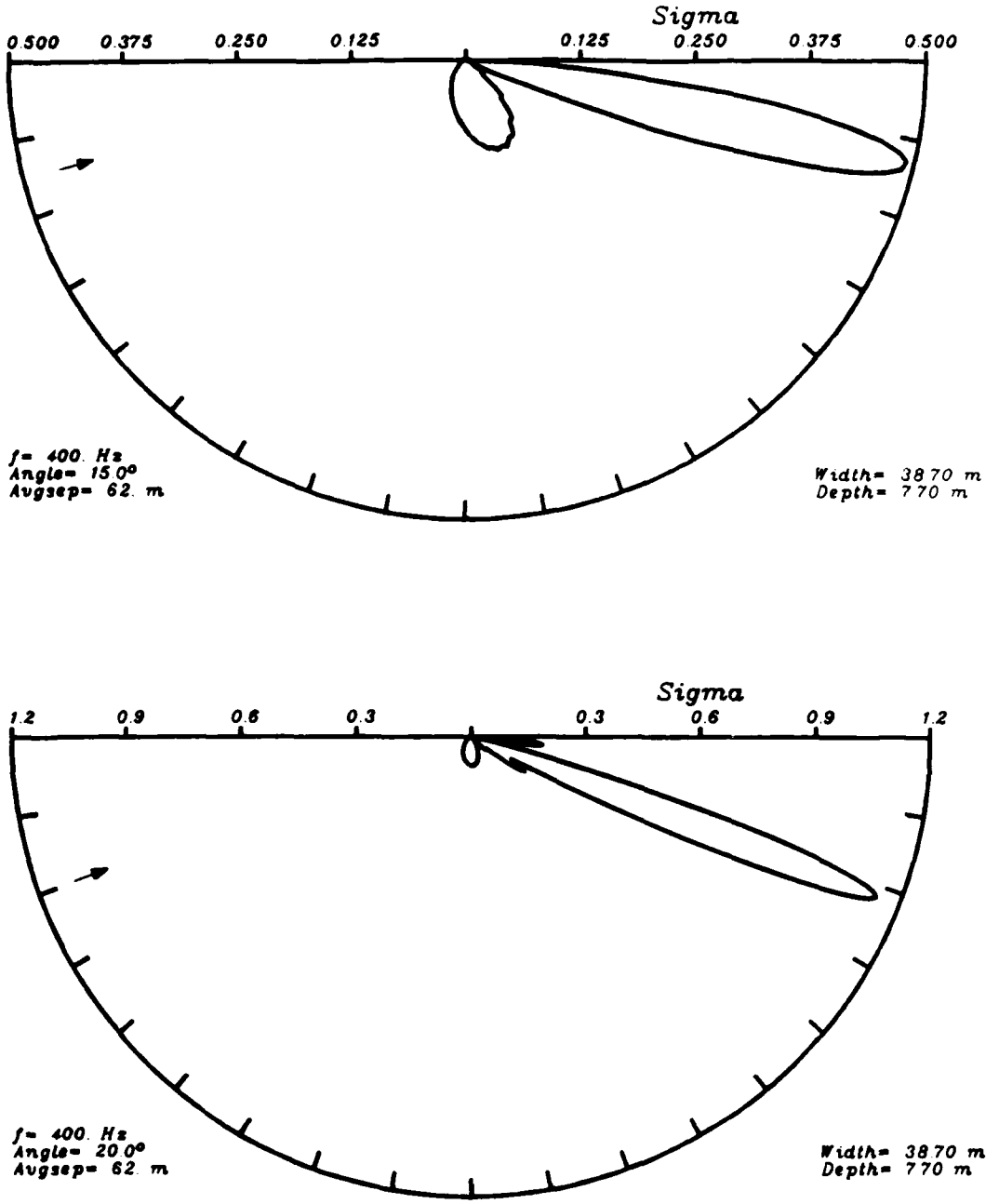

Figure 4.22. (Continued)

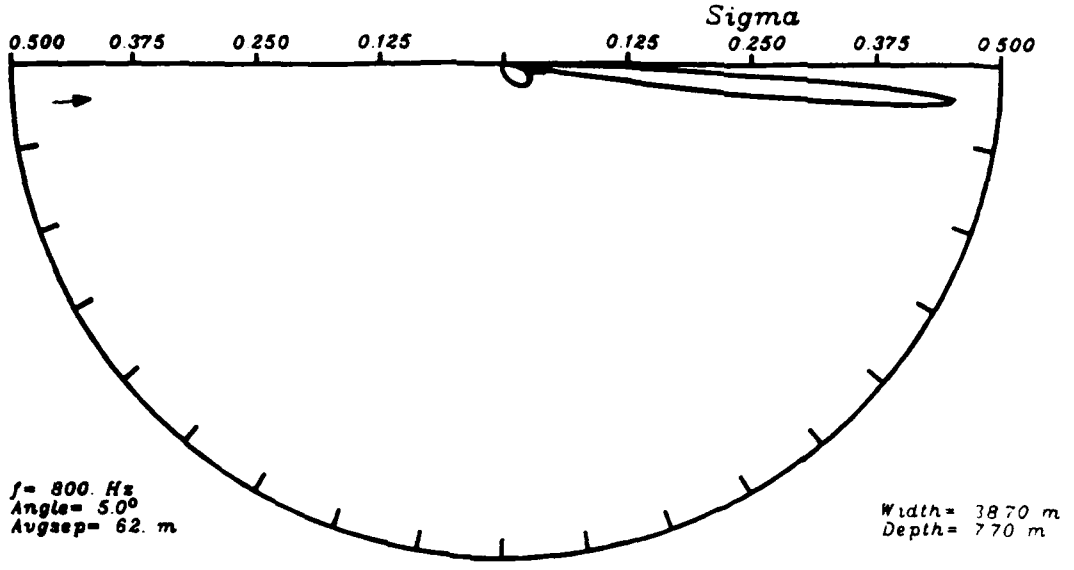

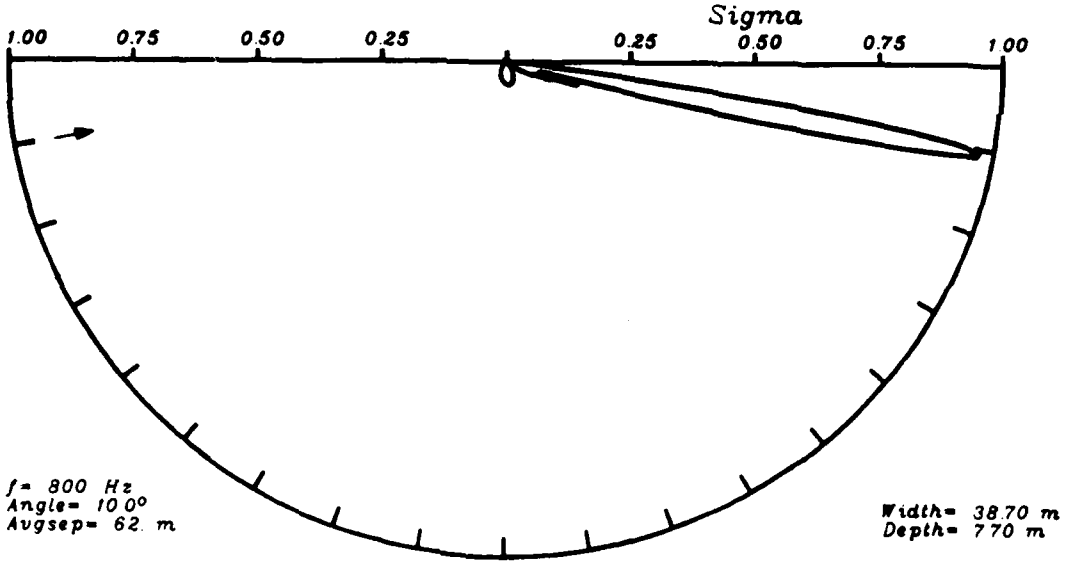

Figure 4.23. As in Figure 4.15, but at 800 Hz.

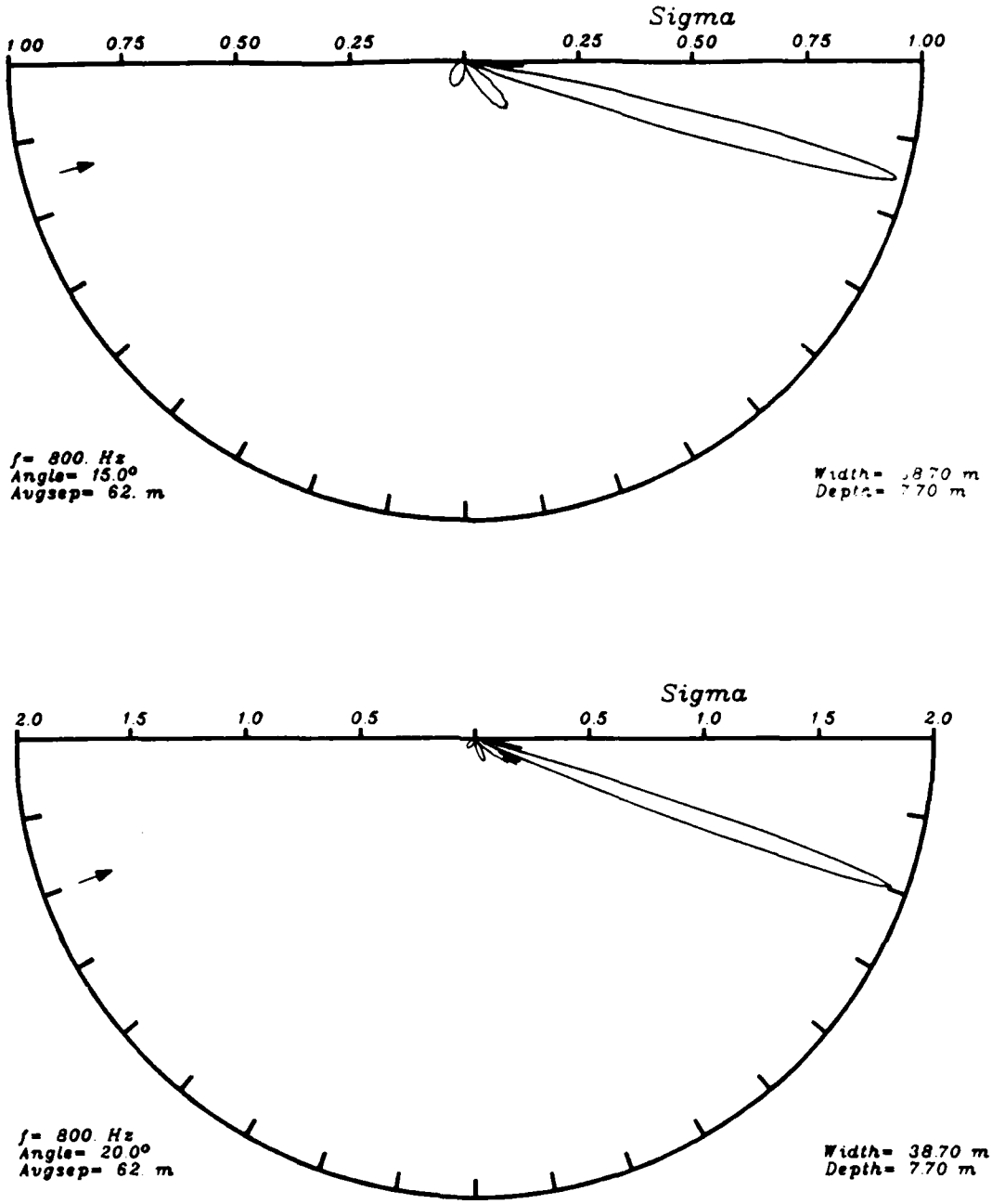

Figure 4.23. (Continued)

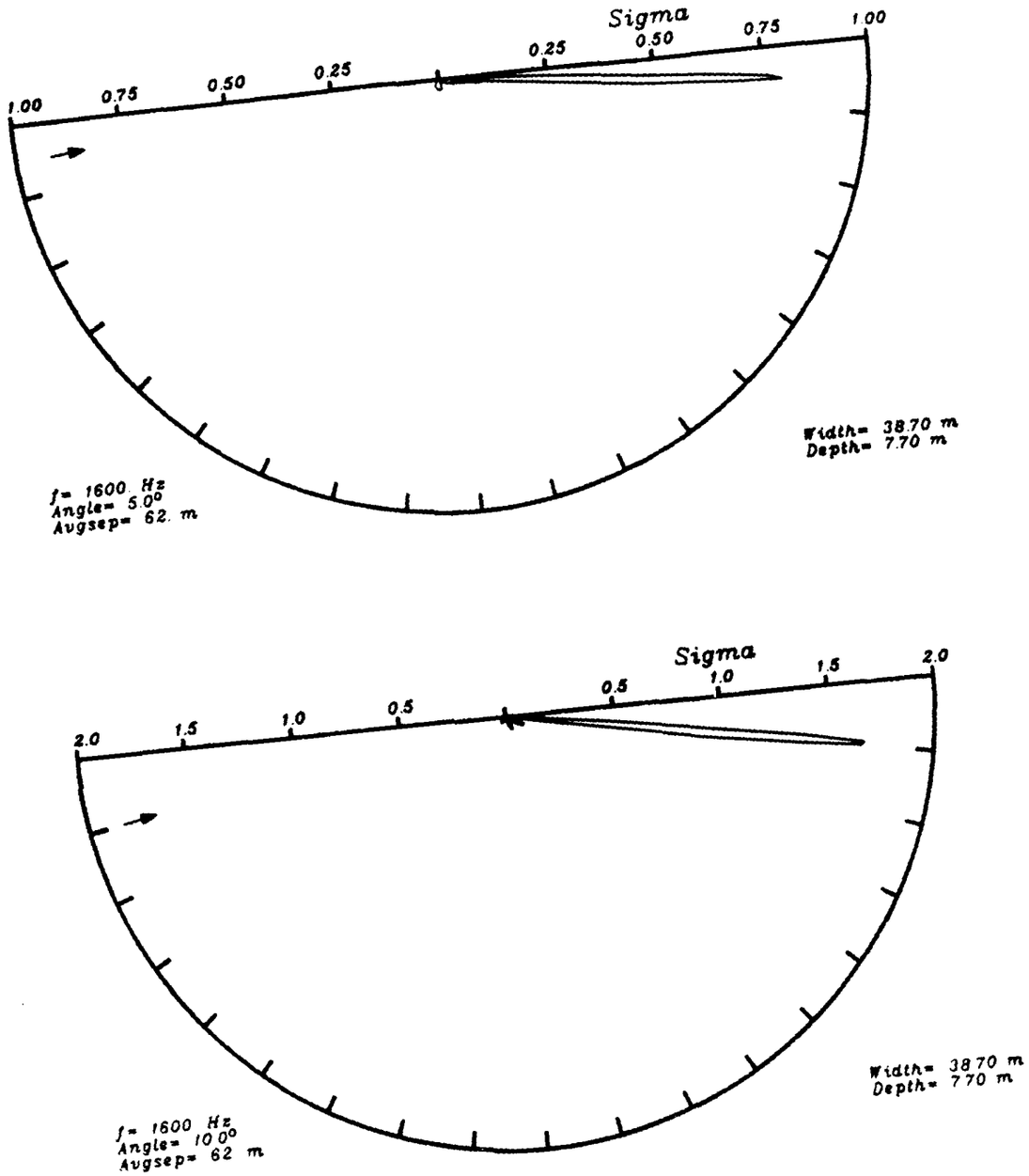

Figure 4.24. As in Figure 4.15, but at 1600 Hz.

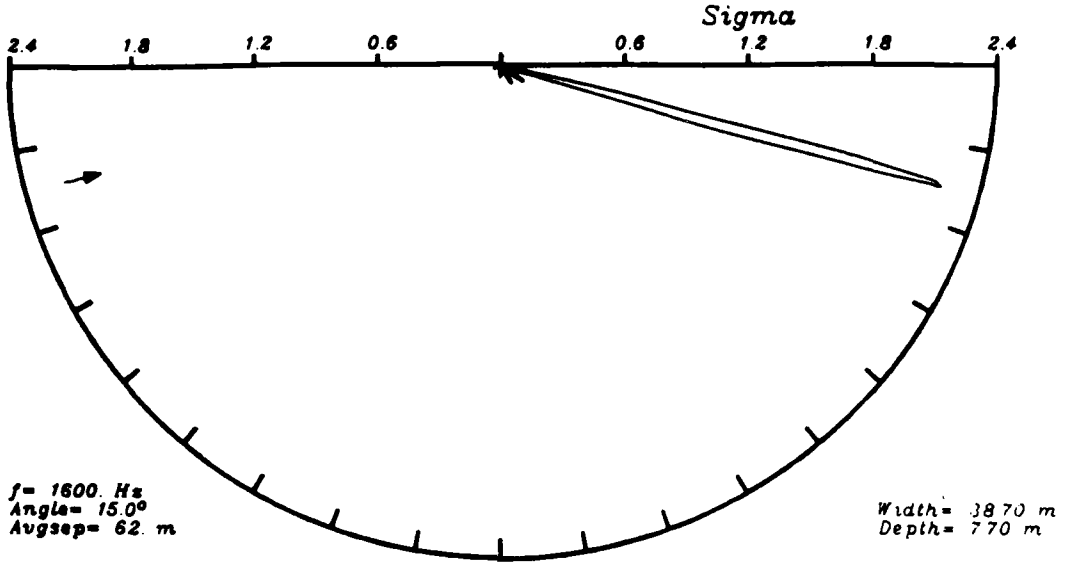

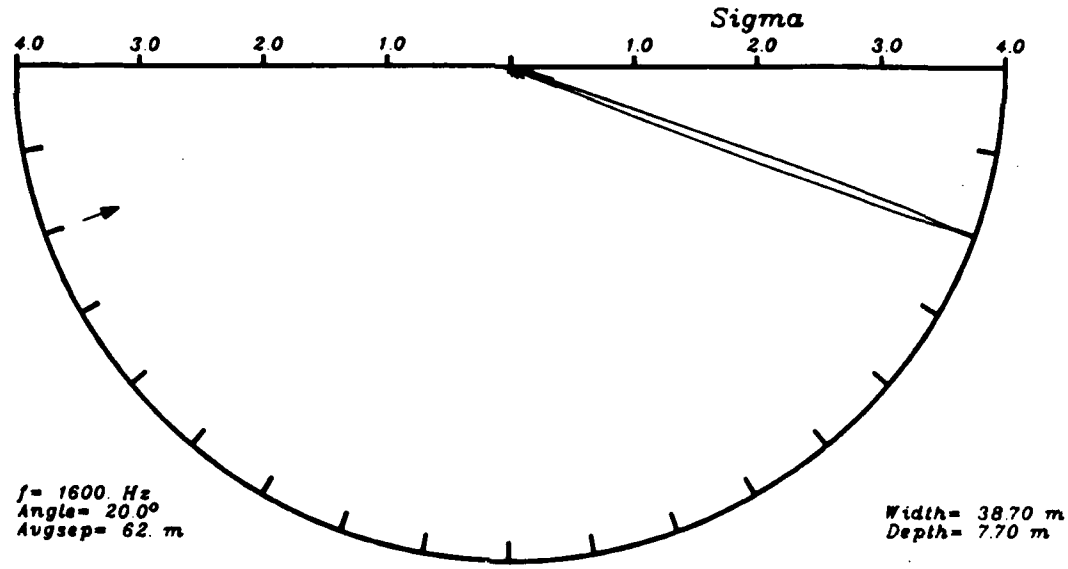

Figure 4.24. (Continued)

REFERENCES

Abramowitz, M., and I.A. Stegun (Eds.), 1964: Handbook of Mathematical Functions. NBS App. Math. Ser. 55, U.S. Govt. Printing Off., Washington, D.C.

Burke, J.E., and V. Twersky, 1964: On scattering by an elliptic cylinder and by a semi-elliptic protuberance on a ground plane. J. Opt. Soc. Am., 54, 732-744.

Burke, J.E., and V. Twersky, 1966: Scattering and reflections by elliptically striated surfaces. J. Acoust. Soc. Am., 40, 883-895.

Clemm, D.S., 1969: Characteristic values and associated solutions of Mathieu's differential equations. Comm. ACM, 12, 399-407.

Diachok, O.I., 1976: Effects of sea-ice ridges on sound propagation in the Arctic Ocean. J. Acoust. Soc. Am., 59, 1110-1120.

Greene, R.R., and K.E. Bowen, 1983: "Introduction to the Arctic environment. Environmental conditions relevant to acoustic propagation and modeling." SAI-84-232-WA, 67 pp.

Greene, R.R., 1984: "Ice statistics and acoustic scattering in the Arctic Basin." SAI-84/1132.

Greene, R.R., and D.M. Rubenstein, 1986: Models of under-ice scattering. To be submitted to J. Acoust. Soc. Am.

Morse, P.M., and H. Feshback, 1953: Methods of Theoretical Physics, McGraw-Hill, New York.

Rubenstein, D., M. Blodgett, and R. Keenan, 1986: "HP 9020 Arctic Modeling Capability." SAIC-86/1906.

END

12-86

DTIC